



HAL
open science

From sink to source: using offshore thermochronometric data to extract onshore erosion signals in Namibia

Mark Wildman, Kerry Gallagher, David Chew, Andrew Carter

► To cite this version:

Mark Wildman, Kerry Gallagher, David Chew, Andrew Carter. From sink to source: using offshore thermochronometric data to extract onshore erosion signals in Namibia. *Basin Research*, 2021, 33 (2), pp.1580-1602. 10.1111/bre.12527. insu-03009369

HAL Id: insu-03009369

<https://insu.hal.science/insu-03009369>

Submitted on 17 Nov 2020

HAL is a multi-disciplinary open access archive for the deposit and dissemination of scientific research documents, whether they are published or not. The documents may come from teaching and research institutions in France or abroad, or from public or private research centers.

L'archive ouverte pluridisciplinaire **HAL**, est destinée au dépôt et à la diffusion de documents scientifiques de niveau recherche, publiés ou non, émanant des établissements d'enseignement et de recherche français ou étrangers, des laboratoires publics ou privés.

1

2 DR MARK WILDMAN (Orcid ID : 0000-0001-9402-7164)

3 DR KERRY GALLAGHER (Orcid ID : 0000-0002-8124-6242)

4

5

6 Article type : Original Article

7

8

9 **From sink to source: using offshore thermochronometric data to extract**
10 **onshore erosion signals in Namibia**

11 Mark Wildman^{1a*}, Kerry Gallagher¹, David Chew², and Andrew Carter³

12 1. Géosciences Rennes, Université de Rennes 1, Rennes, 35000, France.

13 2. Department of Geology, Trinity College Dublin, College Green, Dublin 2, Ireland.

14 3. Department of Earth and Planetary Sciences, Birkbeck University of London, Kathleen
15 Lonsdale Building, Gower Place, London, UK

16 a. Now at School of Geographical and Earth Sciences, College of Science and Engineering,
17 University of Glasgow, Gregory Building, Glasgow, G12 8RZ, Scotland

18 * - Corresponding Author: Mark.Wildman@Glasgow.ac.uk

This article has been accepted for publication and undergone full peer review but has not been through the copyediting, typesetting, pagination and proofreading process, which may lead to differences between this version and the [Version of Record](#). Please cite this article as [doi: 10.1111/BRE.12527](https://doi.org/10.1111/BRE.12527)

This article is protected by copyright. All rights reserved

19 **ABSTRACT**

20 **Products of onshore passive continental margin erosion are best preserved in offshore**
21 **sedimentary basins. Therefore, these basins potentially hold a recoverable record of the**
22 **onshore erosion history. Here, we present apatite fission track (AFT) data for 13 samples**
23 **from a borehole in the southern Walvis basin, offshore Namibia. All samples show AFT**
24 **central ages older or similar to their respective stratigraphic ages, while many single grain**
25 **ages are older, implying none of the samples has been totally annealed post-deposition.**
26 **Furthermore, large dispersion in single grain ages in some samples suggests multiple age**
27 **components related to separate source regions. Using Bayesian mixture modelling we classify**
28 **single grain ages from a given sample to particular age components to create ‘subsamples’**
29 **and then jointly invert the entire dataset to obtain a thermal history. For each sample, the**
30 **post-depositional thermal history is required to be the same for all age components, but each**
31 **component (‘subsample’) has an independent pre-depositional thermal history. With this**
32 **approach we can resolve pre- and post-depositional thermal events and identify changes in**
33 **sediment provenance in response to the syn- and post-rift tectonic evolution of Namibia and**
34 **southern Africa. Apatite U-Pb and compositional data obtained during the acquisition of**
35 **LA-ICP-MS FT data are also presented to help track changes in provenance with time. We**
36 **constrain multiple thermal events linked to the exhumation and burial history of the**
37 **continental and offshore sectors of the margin over a longer timescale than has been possible**
38 **using only onshore AFT thermochronological data.**

39 **Keywords: Numerical modelling, Namibian passive margin, tectonics and sedimentation,**
40 **thermochronology.**

41 Introduction

42 The relationship between onshore erosion and the deposition of the products in sedimentary basins
43 ('source-to-sink') has been the subject of many studies over the last 20 years or so (see Helland-
44 Hansen et al. (2016) for an overview). Due to the implicitly destructive nature of onshore erosion,
45 most studies have focussed on the sink, or sedimentary record, either by quantifying preserved
46 sediment volumes over time as a proxy for erosion (e.g. Leturmy et al., 2003; Rouby et al., 2009),
47 or by using detrital geochronological/geochemical data to fingerprint source regions and constrain
48 'source-to-sink' lag-times (e.g. Bernet and Garver, 2005; Whitchurch et al., 2011). In geological
49 settings that have experienced rapid and deep erosion (c. 6–12 km) (e.g. convergent mountain
50 belts) geo- or thermochronometers with high closure temperatures such as zircon U-Pb (>900°C)
51 (Lee et al., 1997, Cherniak and Watson, 2001) and zircon fission track (ZFT) analysis (closure
52 temperature: $240 \pm 50^\circ\text{C}$) (Hurford, 1986, Bernet, 2009) are typically employed to investigate
53 crustal formation, thermal evolution and sediment routing from the mountain range to the basin.
54 Passive margin settings, however, tend to experience lower magnitudes of erosion, often with
55 protracted or multi-phase erosional histories (Moore et al., 1986; Cogné et al., 2011; Ksienzyk et
56 al., 2014; Wildman et al., 2016; Amidon et al., 2016), the details of which are not resolvable with
57 the higher temperature systems. The Namibian sector of the southwest African 'passive' margin is
58 a prime example of complex, multi-phase, margin evolution. Fully resolving the landscape
59 evolution of the Namibian margin and linking this to the development of offshore sedimentary
60 basins remains challenging.

61 Apatite fission track (AFT) thermochronology provides information on cooling through a
62 relatively low temperature sensitivity range (60–120°C). The application of this technique to
63 outcrop samples has been used to obtain detailed information on onshore passive margin erosion
64 histories, which have been correlated with sedimentary basin stratigraphy/sedimentation rates in
65 passive margin settings (e.g. Gallagher and Brown, 1999; Tinker et al., 2008a). Although detrital
66 AFT analysis has been applied in convergent settings (e.g. van der Beek et al., 2006; Homke et al.,
67 2010; Dunn et al., 2017) its use has been limited along passive margins (e.g. Clift et al., 1996). A
68 major obstacle to using AFT analysis on detrital apatite is introduced if the apatite has been
69 partially annealed during post-depositional heating, typically caused by burial. If the detrital
70 apatite is heated such that all pre-depositional tracks are annealed, the AFT data will only reflect
71 post-depositional thermal events. If the detrital apatite experiences no annealing after deposition,

72 the AFT data will retain the record of the pre-depositional history. Partial annealing will modify
73 the AFT record of the pre-depositional in the detrital apatite. Recovering this record becomes
74 more complicated if a sample is comprised of apatites derived from multiple sources with different
75 pre-depositional thermal histories. By addressing this problem, we can potentially identify onshore
76 erosion events that have been removed from the onshore AFT record.

77 The temporal resolution of thermal histories constrained by onshore AFT is limited depending on
78 the timing and magnitude of erosion. If a phase of erosion causes a rock to cool rapidly from
79 temperatures hotter than the AFT closure temperature ($110 \pm 10^\circ\text{C}$) then the AFT data will record
80 that cooling event and, potentially, subsequent lower temperature events in the thermal history.
81 However, due to total track annealing the AFT data will have no information on earlier thermal
82 events (Malusà and Fitzgerald, 2019). In the context of passive margin evolution this means that if
83 the total magnitude of erosion during the post-rift history was large enough (e.g. typically > 4 km)
84 to cool rocks from hotter than $110 \pm 10^\circ\text{C}$ to the surface then these surface samples will not record
85 syn-rift or earlier related cooling. In other words, the AFT data from single onshore surface
86 samples can only provide thermal history information back to the time when that sample cooled
87 through the AFT closure temperature. To infer the earlier syn-rift thermal history, high
88 temperature systems (e.g. ZFT or zircon (U-Th)/He) may be used on the same outcrop sample.
89 However, the resolution of the thermal events will depend on initial starting temperatures of the
90 rock prior to the onset of break-up exhumation. Alternatively, we propose this information can be
91 recovered from the detrital AFT record, provided the host sediments have not been heated above
92 the total annealing temperature.

93 Here, we present an AFT dataset from a borehole, offshore of Namibia in the south Atlantic (Fig.
94 1). As a consequence of low burial-related maximum temperatures, the samples have preserved a
95 record of their onshore (i.e. pre-depositional) thermal history. Despite considerable dispersion in
96 the single grain age data, we show that some of this onshore thermal history signal can be
97 extracted, as well as the post-depositional thermal evolution. The results imply that the offshore
98 sediments record rapid erosion at the time of rifting, a signal not obvious in the AFT data from
99 onshore surface samples. As detailed below, the AFT dataset combines single grain ages collected
100 using the long-established external detector method (EDM) and ages collected using the new LA-
101 ICP-MS method and provides an opportunity to directly assess the comparability of the two
102 approaches.

103 **Geological setting**

104 The basement in Namibia comprises Palaeoproterozoic and Meso- to Neoproterozoic gneisses and
105 supracrustal rocks (Kroner et al., 2004) (Fig. 1a). On top of the basement are the siliciclastic-
106 carbonate successions of the Damara Supergroup, which experienced high P-low T metamorphism
107 along the southern branch of the intracontinental Damara metamorphic belt during Pan-African
108 (600–480 Ma) orogenesis (Miller, 1979). The central Damara orogen experienced low P–high T
109 contact metamorphism associated with the emplacement of voluminous granitic plutons at 540–
110 500 Ma (Jung et al., 2019, 2020).

111 The tectonic structure of the Damara Orogen is characterised by NNW-trending transpressional
112 faults of the northern Kaoka and southern Gariep Belts and the ENE-trending structures in the
113 main central Damara Belt that formed during Pan-African convergence between the Congo and
114 Kalahari cratons (Passchier et al. 2002; Frimmel, 1995; Miller, 1983). Major NE-SW trending
115 tectonic lineaments define the regional structural trend in the Damara Belt. These are believed to
116 reflect major, reactivated NE-SW trending structures within the pre-Damara metamorphic
117 basement that controlled the location of Damara Supergroup sedimentation in rift basins (Tankard
118 et al., 1982). The Pre-cambrian tectonic framework in Namibia, as elsewhere in Africa, has had a
119 major influence on Phanerozoic tectonic events (Clemson et al., 1997; Holzförster et al., 1999;
120 Raab et al., 2002; Salazar-Mora et al., 2018; Will and Frimmel, 2018).

121 The Permo-Triassic sedimentary rocks of the Karoo Supergroup, which cover much of the
122 southern African interior, are only present in sporadic fault-bounded outliers in Namibia (Fig. 1a).
123 Jurassic–Early Cretaceous clastic sediments were sourced from the local basement and were likely
124 deposited in syn-rift fault-bounded basins. The Early Cretaceous Etendeka flood basalts cover
125 these sediments (Fig. 1a) and have been dated at 134–127 Ma, which is coeval with the Parana
126 flood basalts in NE Brazil (e.g. Gibson et al., 2006). This large igneous province is attributed to
127 magmatic processes associated with West Gondwana passing over the Tristan da Cunha hotspot
128 (O'Connor et al., 2012; Hoernle et al., 2015), contemporaneous with the northward-propagating
129 breakup of South America from Africa. The onshore post-rift geology is limited to minor alkaline
130 intrusions and thin (0–400 m) terrestrial Cenozoic deposits of the Kalahari Group that thicken
131 toward the northeast (Ward, 1988; Ward and Martin, 1987; Marsh, 2010; Wanke and Wanke,
132 2007).

133 Onshore, the present-day Namibian margin topography is dominated by a broadly coast-parallel
134 escarpment zone lying c. 80–100 km inland from the present-day coastline (Fig. 1b). The
135 escarpment marks the transition from a low-lying, low-relief coastal zone to an elevated (c. >1
136 km), low-relief interior plateau. The coastal escarpment varies along its length becoming more
137 prominent and characterised by higher relief in places, while in others it diminishes and is harder
138 to define from the increasing elevation of the gently convex-up sloping coastal zone. The elevated
139 plateau is a dominant and enigmatic feature that spans the continental interior of southern Africa.
140 Immediately inland of the escarpment the plateau has a concave-up sloping profile with decreasing
141 elevation over c. 100–200 km. The Swakop river valley follows the structural trend (ENE) of the
142 Okahanja Lineament and Damara Metamorphic Belt (Fig. 1b) and bounds the region of highest
143 elevations to the north. Sporadic inselbergs linked to Early Cretaceous alkaline intrusions (e.g.
144 Brandberg) form local points of high elevation along the margin (Fig. 1b).

145 Offshore, the stratigraphy preserved in the Walvis and Orange Basins are a direct product of
146 geological processes and the delivery of sediments during erosion that formed the topography of
147 southwestern Africa (Fig. 1c). Borehole 2213/6-1 was drilled into the Koigab Fault zone in the
148 Walvis Basin (Clemson et al., 1997), which is a structural high relative to the main Walvis Basin
149 to the west. The Koigab Fault Zone is part of the Namib Rift, which initiated in the Carboniferous-
150 Permian, and was an extensional fault system until inversion and erosion during the mid-Triassic.
151 The well log of the borehole shows interbedded sequences of claystone and fine- to coarse-grained
152 sandstone overlying layered units of continental volcanic rocks and siliciclastic sediments. These
153 are likely related to the emplacement of Etendeka lavas and onshore erosion during the syn-rift
154 phase, respectively, and are comparable to the wedges of interlayered basalts and aeolian sands
155 observed at the Kudu gas field in southern offshore Namibia (de Vera et al., 2010).

156 The general stratigraphy of the Walvis Basin is summarised in Fig. 1c and discussed in greater
157 detail by Holtar and Fosberg (2000) and Baby et al. (2018). Post-rift successions overly a rifted
158 continental basement with Late Jurassic to Early Cretaceous siliciclastic and volcanic rocks
159 deposited in N-S trending syn-rift grabens (Clemson, 1997; Clemson et al., 1999, Light et al.,
160 1993). The stratigraphy of the mid-Late Cretaceous and Cenozoic post-rift sequences in the
161 Walvis Basin is dominated by siltstones, claystones and minor sandstone interbeds that were
162 deposited in marine shelf, slope and basin environmental settings and which imply significant
163 post-rift erosion has occurred (Clemson et al., 1997; Holtar and Fosberg, 2000; Baby et al. 2018).

164 The Late Cretaceous succession also exhibits large-scale gravity driven fault structures, which are
165 associated with episodic gravitational collapse driven by uplift of the onshore domain in the Late
166 Cretaceous (de Vera et al., 2010). The boundary between the syn-rift and post-rift sequences is the
167 Late Hauterivian (132.9 ± 2 to 129.4 ± 1.5 Ma) breakup unconformity (Light et al., 1993; Baby et
168 al., 2018). Additional unconformities are observed in the lower Campanian (c. 81 Ma), top
169 Maastrichtian (c. 66 Ma), middle Oligocene (c. 30 Ma) and upper Miocene (c. 11 Ma) (Fig. 1c)
170 (Baby et al., 2018).

171 During the Early Cretaceous (c. 130–113 Ma) initial post-rift phase, the Walvis Basin accumulated
172 an estimated 1.04×10^4 km of sediment (Baby et al., 2020). The largest volumes of sediment were
173 deposited during the mid-Late Cretaceous (23.15×10^4 km) (Baby et al., 2018) with c. 3 km of
174 sediment deposited in the vicinity of the borehole location over this time (Baby et al., 2020).
175 Cenozoic sediment volumes are estimated to be 8.79×10^4 km with a thickness of up to c. 1800 m
176 in the main depocenter of the basin and c. 600 m in the vicinity of the borehole (Baby et al., 2018).

177 **Apatite Fission Track Thermochronology**

178 **Methods**

179 Apatite fission-track data were obtained from 13 samples from cuttings, over a depth range of
180 650–2555 m, from borehole 2213/6-1 (Fig. 1). The AFT data we present here are a composite
181 dataset comprised of currently unpublished data collected in the 1990s (dataset referred to as AFT-
182 90, SI-Table 1) and new LA-ICP-MS AFT data collected for this study (SI-Table 2 and 3). The
183 new data were collected on the same grain mounts as the AFT-90 dataset although not necessarily
184 on the same grains.

185 The AFT-90 age data (SI-Table 1) were acquired using EDM (Hurford and Green, 1983) and 20–
186 21 grains were dated for all samples. The dataset includes horizontal confined track (CT) lengths
187 and c-axis angles but no composition or proxy (Dpar) measurements. These data were used to
188 demonstrate multi-sample inverse thermal history modelling by Gallagher (2012) (see Fig. 10 in
189 Gallagher, 2012).

190 New AFT age data were acquired using the LA-ICP-MS protocol described by Chew et al. (2012)
191 and Cogné et al. (2020) (SI-Table 2 and 3). Fission tracks were counted using a Zeiss AxioImager
192 M1m microscope and Autoscan Fission Track Studio software. Additional horizontal and inclined

193 (corrected for dip angle in Fission Track Studio) CTs were also measured, but only in grains that
194 were counted so that track lengths can be directly associated with an AFT age. Five Dpar
195 measurements were made on each counted grain as a proxy for compositional influence on
196 annealing for each counted grain. Chlorine content was also measured on each analysed grain
197 following the protocol described by Chew et al. (2014a) as well as additional compositional data
198 for which a subset of elements (e.g. Sr, Y, LREEs [La, Ce, Pr and Nd]) is presented in SI-Table 3.
199 For each grain ablated for FT analysis, we obtained an apatite U-Pb age (e.g. Cogne et al., 2020;
200 Chew et al., 2014b) and we also obtained additional U-Pb age data on randomly selected apatite
201 grains in several of the borehole samples (SI-Table 3).

202 The AFT-90 data and new LA-ICP-MS AFT data have similar AFT ages and track length data
203 (Fig. 2a, c). The age difference between the two datasets (age difference = AFT-90 central age/
204 LA-ICP-MS central age) is 0.60–1.00 and although the AFT-90 central ages are typically younger
205 than the LA-ICP-MS AFT central ages, nine out of the 13 samples overlap within uncertainty of
206 the 1 to 1 relationship line. There is no correlation between these small age discrepancies between
207 the two datasets and the central AFT age or composition (Fig. 3). However, there appears some
208 correlation between the larger age differences between the two datasets and the single grain age
209 dispersion, particularly for the AFT-90 dataset (Fig. 2b). The degree of single grain age dispersion
210 is similar for the AFT-90 and LA-ICP-MS age dataset with average dispersion of 35% and 40%
211 respectively. In some cases, the LA-ICP-MS AFT datasets lowers the amount of age dispersion
212 (e.g. MT2353) and in others it increases the age dispersion (e.g. MT2355). This can be
213 interrogated further using radial plots (Fig. 3) or the classical χ^2 statistic (see SI-Table 1 and SI-
214 Table 2). It is apparent that the number of grains counted in the AFT-90 study were generally
215 insufficient to characterise the amount of single grain age dispersion in the samples. Moreover, the
216 difference between the EDM and LA-ICP-MS age seems to increase in samples with greater age
217 dispersion. This may be attributed to the relative precision associated with measuring U content by
218 counting induced tracks with the EDM method versus measuring U directly via laser ablation.
219 AFT ages collected using EDM and LA-ICP-MS AFT approaches are generally considered to be
220 consistent (*cf.* Seiler et al., 2014, Cogné et al., 2020). While more comparison datasets will be
221 required to robustly justify this assumption. Given this assumption, we present all the age data as a
222 single dataset (Table 1).

223 To facilitate the integration, plotting, and modelling of the EDM age data with the LA-ICP-MS
224 age data, we determine an equivalent value for the number of induced tracks (N_i) for each grain
225 dated using LA-ICP-MS based on the measured LA-ICP-MS AFT age and its uncertainty and
226 employing the zeta calibration factor, ρ_d and N_d (track density and number of tracks counted for
227 the U dosimeter) from the AFT-90 EDM analyses.

228 **Results**

229 The combined data set shows central AFT ages from 90.2 ± 3.5 to 317.0 ± 33.0 Ma (Table 1). All
230 samples fail the χ^2 test at the 5% level and have large dispersion (23–82%). Mean track lengths
231 (MTLs) range from 10.45 ± 0.18 to 12.70 ± 0.11 μm and decrease with depth, a trend that is
232 consistent with some partial annealing post-deposition (Table 1). Track length distributions
233 (TLDs) are unimodal and generally fairly broad and normally distributed. Some TLDs show slight
234 tails of short (< 12 μm) tracks (see SI-1 for TLDs).

235 The dispersion of single grain ages and the presence of multiple age populations is more
236 pronounced in radial plots (Fig. 3) for some samples (e.g. MT2352) more than others (e.g.
237 MT2357). The compositional proxy, D_{par} , available for the new data only, typically does not
238 show any clear relationship with the AFT ages, suggesting that composition is not the dominant
239 control on the dispersion. For MT2352, it is clear that the older component has larger D_{par} .
240 However, given the very large disparity in ages and the present day shallow crustal (i.e. low
241 temperature) position of the sample, it is plausible that the dispersion represents distinct pre-
242 deposition erosion histories leading to a mixture of age populations. Our measured Cl wt% values
243 are generally positively correlated with D_{par} (see SI-2) and although this is likely to be the
244 dominant compositional influence on fission track annealing (Barbarand et al., 2003) we use D_{par}
245 in the modelling as a proxy to constrain the bulk compositional influence on track annealing.

246 Pan-African (c. 600–500 Ma) apatite U-Pb ages are dominant in every sample. Deeper than -1410
247 m (i.e. samples MT2354 to MT2363) almost all ages are Pan-African with only occasional grains
248 showing older Proterozoic ages or younger Permo-Triassic (i.e. Karoo) ages. Shallower than -1410
249 m (i.e. MT2353 to MT2351), there is a greater diversity of ages, with the clear Pan-African signal
250 mixed with a larger abundance of Meso- to Neoproterozoic (c. 1.5–0.8 Ga) ages and, particularly
251 for MT2352, a significant number of Palaeoproterozoic to Archean (i.e. >2 Ga) ages (see SI-Table
252 3).

253 Following the approach of O'Sullivan et al. (2020) we plot the data on a Sr/Y vs. Σ LREE biplot to
254 determine the general source lithology of detrital apatite (Fig. 4a). The majority of the grains can
255 be traced to high-grade metamorphic rocks and some to low- to medium grade metamorphic rocks
256 (Fig. 4b, c). A small cluster of points are observed in the top right of the plot suggest a source
257 comprising of ultramafic rocks and alkaline-rich igneous rocks. This cluster clearly correlates with
258 the oldest apatite AFT ages and U-Pb ages (Fig. 4b, c).

259 Given the comments above, we assume that the dispersion in all samples reflects a mixture of
260 different provenance related or pre-depositional thermal history signals. Carter and Gallagher
261 (2004) showed provenance information can be obtained from samples that have undergone post-
262 depositional annealing, especially where the pre-deposition history involved protracted cooling as
263 indicated by the presence of Palaeozoic AFT ages in our samples. In an attempt to extract these
264 signals, we first use AFT mixture modelling to identify discrete age components for each sample.
265 Then we assign each measured single grain age to the most probable age component to define
266 'subsamples' to be used for inverse thermal history modelling. These subsamples also incorporate
267 any track length data associated with the assigned single grain ages.

268 *Mixture modelling*

269 The transdimensional Bayesian mixture modelling approach presented by Jasra et al. (2006) is
270 used to identify the number of age components in each sample. In this approach, we obtain a
271 probability distribution on the number of components. This avoids needing to specify in advance
272 the number of components, and instead we choose the most probable number of components. We
273 can also classify each of the measured single grain AFT ages into a given age component based on
274 the probability of a given grain coming from a particular age component. We note that annealing
275 can lead to dispersion in ages such that an initially symmetrical single component age distribution
276 may become asymmetrical and then a skew distribution model is more appropriate than a
277 symmetrical (e.g. Gaussian) component distribution that may lead to an overestimation of the
278 number of components. Therefore, we assume skew-t distributions for the form of the component
279 age distributions. A skew-t distribution (see Jasra et al, 2006) is defined by the location and scale
280 parameters (similar to the mean and standard deviation) with two additional parameters defining
281 the left and right skewness. The Gaussian distribution is a special case of the skew-t distribution
282 for which the two skewness parameters are equal and large. The final parameter is the proportion

283 of an age component contributing to the overall combined distribution. Given the parsimonious
284 nature of Bayesian inference, the approach we adopt also tends to prefer less rather than more
285 components. However, inferring too many age components may not present a problem as we
286 would expect the thermal histories to be similar, for example, if two inferred components really
287 come from just one.

288 We ran $1-2 \times 10^6$ iterations of the Markov chain Monte Carlo sampler. As explained in more detail
289 by Jasra et al. (2006 and references therein), the inference of age components is based on
290 modelling the unknown, 'true' ages, rather than the measured ages (which have measurement
291 uncertainty). In practice, this means for each measured age, we resample an age from a Gaussian
292 distribution with a mean equal to the measured age and a standard deviation equal to the
293 measurement uncertainty. The set of resampled ages are then used for the inference of age
294 components at each iteration. At the end of the sampling iterations, we choose the maximum of the
295 posterior probability distribution on the number of components (Fig. 5). Given this maximum
296 posterior estimate, we construct a predicted distribution for each age component, weighted by the
297 estimated proportion, using the expected values for the mean and standard deviation. From these,
298 we can choose the age component distribution that yields the maximum probability for a measured
299 single grain age from both the AFT-90 and LA-ICP-MS data sets and allocate the measured single
300 grain age to that component (Fig. 5).

301 We did not include track lengths measured in the original AFT-90 analysis because they do not
302 have an associated measured grain age. However, all track lengths and Dpar values from the new
303 LA-ICP-MS dataset were measured on grains that were also dated, so we can also assign length
304 and Dpar measurements to a specific age component for each sample. Therefore, for any sample
305 with multiple components, we create 'subsamples' that have a track length distribution, a
306 distribution of Dpar values, defined by a mean and standard deviation, and single grain ages
307 assigned to a discrete component (based on both the AFT-90 and LA-ICP-MS age data) (Fig. 6,
308 SI-Table 4).

309 **THERMAL HISTORY MODELLING**

310 *Model set-up*

311 Thermal history modelling was performed using a Bayesian multi-sample vertical profile
312 inversion approach (Gallagher, 2012). The methodology behind this approach has been described
313 in detail in Gallagher et al. (2005) and Gallagher (2012) but, to summarise, we take a suite of
314 samples at different depths (as in our borehole dataset) and look for a general thermal history,
315 including palaeotemperature gradients, that can adequately predict the data for all samples.

316 All samples are terrigenous siliciclastic sediments composed of material transported from the
317 onshore Namibian continental margin. Due to a paucity of fossil material, their stratigraphic ages
318 are not well defined (Fig. 7, Table 1). Consequently, each sample is assigned a loose stratigraphic
319 time-temperature constraint, sampled from uniform distributions for a range in the time of
320 deposition and a temperature of $10 \pm 10^\circ\text{C}$. During the inversion runs, the stratigraphic age for
321 each sample is drawn from these prior distributions. Present-day temperature constraints were
322 estimated from downhole temperature (corrected BHT) data. These are consistent with a
323 geothermal gradient of $25 \pm 5^\circ\text{C}/\text{km}$ and a surface temperature of around 4°C . The palaeo-
324 temperature gradient was assumed to be constant over time, but the actual value was allowed to
325 vary between $25 \pm 10^\circ\text{C}/\text{km}$. No other constraints, such as possible episodes of erosion inferred
326 from unconformities observed in the main depocenters of the basin (e.g. Fig. 1c), are imposed on
327 the model. Instead we let the data decide when episodes of heating and cooling are required and
328 discuss the implications of these thermal events below alongside observations from the offshore
329 stratigraphy.

330 As described above, we combined the old and new AFT age data for each sample, used mixture
331 modelling to identify age components, classified each single grain age to a given age component
332 and extracted the track length measurements and Dpar values associated to those single grain ages
333 (from the new AFT data) to form a subsample. For thermal history modelling, we adopted the
334 multi-compositional fission-track annealing model of Ketcham et al. (2007). We allowed Dpar to
335 vary during the inversion runs, resampling values from a normal distribution, with the mean and
336 standard deviation equal to the mean and standard deviation of all Dpar measurements for each
337 subsample. Letting the compositional proxy vary in this way provides some flexibility in the
338 modelling to allow for the dispersion in the measured Dpar values, and the fact that the annealing
339 models have inherent uncertainty in their construction and calibration.

340 All subsamples from a given sample were required to have the same post-depositional thermal
341 history. However, we allowed each subsample to have an independent pre-depositional thermal
342 history. To simulate the pre-depositional thermal history, we included an additional independent
343 time-temperature (t-T) point for each subsample, which is required to be before the time of the
344 stratigraphic age constraint. In this way, the pre-depositional thermal history is parameterised as
345 linear cooling from an unknown t-T point (a distribution of which is estimated during the
346 inversion) to the stratigraphic age temperature constraint. This is the simplest parameterisation for
347 the pre-depositional thermal history and will effectively constrain the average rate of cooling over
348 the inferred duration prior to deposition. The predicted fission track age, MTL and TLD will
349 reflect annealing over the pre- and post-depositional portion of the thermal history. The
350 distribution of time-temperature point forming the initial part of the pre-depositional thermal
351 histories can be visualised in 2D plots in SI-3, and in these we often see a trade-off between time
352 and temperature.

353 *Inverse modelling results*

354 The expected thermal history model for the borehole, post-200 Ma (see SI-4 for longer thermal
355 history), is shown in figure 7a, and the summary predictions for this model are given in figure 7b.
356 The overall trends of the measured AFT and MTL subsample data with depth are well reproduced
357 by the model predictions. The maximum post-depositional temperatures are $< 110^{\circ}\text{C}$ for the
358 deepest sample and $< 60^{\circ}\text{C}$ for the shallowest sample. This implies that fission tracks in most, if
359 not all, of the samples have not been totally annealed post-deposition. In other words, the data are
360 potentially providing information about erosion-related cooling prior to deposition. We recover
361 this in a relatively simple way, given the nature of the single time-temperature point
362 parameterisation we adopted.

363 *Pre-depositional thermal histories*

364 The pre-depositional components of the thermal history can be classified into three groups (Table
365 2) (SI-4). Nine subsamples, (Group I) all with relatively old single grain AFT ages, show
366 protracted cooling initiated prior to 150 Ma (Fig. 7a) (see SI-4 for the thermal history beyond 200
367 Ma). Eleven subsamples (Group II) show rapid cooling across the base of the Partial Annealing
368 Zone (PAZ) between 145–125 Ma (Fig. 7a). The three shallowest samples (Group III) show rapid
369 cooling in the Late Cretaceous. Two subsamples show rapid cooling initiating at between 100 and

370 90 Ma and one shows rapid cooling starting at 70 Ma (Fig. 7a). Occasionally pre-depositional
371 thermal history paths can be seen to start in the middle of the PAZ. In these cases, it is implicit that
372 the samples cooled rapidly from temperatures hotter than the bottom of the PAZ just prior to this
373 time.

374 Using each sampled thermal history, we also make a prediction for the AFT closure time (t_c) for
375 each sample component. As track formation occurs at a more or less constant rate over the
376 duration of a thermal history, each track has an effective formation age. In modelling track
377 annealing over time, we follow the approach described by Crowley (1993) in which the thermal
378 history, divided into isothermal time steps of around 1 m.yr., is run backwards in time. This allows
379 us to easily monitor the time when the oldest simulated track is totally annealed. By implication,
380 all tracks present at, and so formed prior to, that time would also have been totally annealed. We
381 refer to this time as the closure time, t_c , and there will be a corresponding temperature at that time
382 in the thermal history, which could be considered as the effective closure temperature. The AFT t_c
383 is then a model calculation and will be older or equal to the measured AFT age. It can be taken as
384 an indication of the maximum time back to which the thermal history can be resolved. It will
385 reflect compositional controls on annealing as these will change the effective closure temperature
386 of the sample. During the inversion iterations, both the thermal history and Dpar can vary, and so
387 we obtain a distribution of AFT t_c that incorporates these variations. We use the average and
388 standard deviation of this distribution as an estimate and uncertainty of AFT t_c for each subsample
389 (Fig. 8).

390 Taking all estimates of AFT t_c for each subsample shows that the dominant population is Early
391 Cretaceous (syn-rift, c. 145–125 Ma) with a smaller population in the Triassic-Carboniferous (c.
392 320–240 Ma) and some sample components making up a mid-late Cretaceous (post-rift, 110–80
393 Ma), a Cambrian-Proterozoic (Pan-Africa, c. 560–500 Ma) and a Neoproterozoic (c. 820–760 Ma)
394 population (Fig. 8). In terms of the downhole trends, the deepest (stratigraphically oldest) sample
395 yields a late Palaeozoic-early Mesozoic t_c (223 ± 25 Ma) indicating that, prior to syn-rift erosion,
396 the rocks containing apatite were already at relatively low temperatures (Fig. 7a, Fig. 8) onshore.
397 With subsequent deposition of more syn-rift sediment, an onshore rift-related rapid cooling signal
398 becomes more dominant (Fig. 7a, Fig. 8). The predicted AFT t_c for the sample components from
399 2460 m (MT2362) to 1410 m (MT2354) depth are around 147 ± 9 to 123 ± 1 Ma, although some
400 of these samples still contain a population of grains with an older (>200 Ma) t_c (Fig. 8). In the

401 shallower samples, e.g. 1120 m (MT2353), this syn-rift signal is no longer apparent but there is a
402 mid-Cretaceous AFT t_c (Fig. 8) caused by rapid pre-depositional cooling at this time (Fig. 7a).
403 This signature is present at 870 m (MT2352), but this sample also apparently records slow cooling
404 since the Proterozoic before deposition in the Late Cretaceous (Fig. 7a). The shallowest sample at
405 650 m (MT2351) also shows a mixed AFT t_c signal (Fig. 8), reflecting the cooling episodes
406 already observed over the Proterozoic and Early Cretaceous as well as a younger Late Cretaceous
407 AFT t_c (Fig. 8) and associated pre-depositional rapid cooling signal (Fig. 7a).

408 *Post-depositional thermal history*

409 The inferred post-depositional thermal history of the borehole profile can be characterised by
410 several stages (Fig. 7a). (i) From approximately 120 Ma, there is a variable rate of heating,
411 initially relatively slow, then from c. 90–65 Ma, there was a phase of accelerated heating bringing
412 the deepest sample from temperatures of 32–48°C to between 92 and 106°C, the maximum
413 palaeotemperatures. Over most of post-depositional thermal history, the geothermal gradient is
414 inferred to be c. 20°C/km but varies occasionally to 25°C/km (e.g. at 80 Ma) and ends at 25°C/km,
415 consistent with the present day measured geothermal gradient as imposed in the prior. Given the
416 range of predicted geothermal gradients, the upper and lower limits of temperature change from
417 90–65 Ma and an assumption of steady state heat transfer, the amount of heating equates to burial
418 under c. 1.8–3.7 km of sediment, or a heating rate of ~1.5–2.0°C/m.y. Coincident with the onset of
419 this mid-Late Cretaceous burial-related heating, is rapid pre-depositional cooling associated with
420 the shallowest samples (clearly yet to be deposited), implying a link between increase in the rates
421 of onshore erosion and offshore deposition at c. 90 Ma. (ii) Following the period of burial related
422 heating, there is a period of rapid cooling around 8–9°C/m.y. in the basin at the end Late
423 Cretaceous/Early Cenozoic (40–45°C during 65–60 Ma), equivalent to around at least 1.6–2.3 km
424 of eroded section. The sediments equivalent to the two youngest/shallowest samples were
425 subsequently deposited in the basin but, in comparison to the deeper samples, their pre-
426 depositional thermal histories reflect older cooling events. (iii) From 60–35 Ma, the entire profile
427 is heated by c. 30°C, or around 1°C/m.y., equivalent to c. 1.2–1.5 km of overburden. (iv) The final
428 thermal event is a period of cooling of around 20°C to bring the samples to their present-day
429 temperatures. This could imply around 0.8–1 km of erosion, but as we discuss below, this inferred
430 cooling may reflect other controls.

431 **DISCUSSION**

432 The inferred thermal history combined with the estimates of AFT t_c for each sample age
433 component reveals information on both onshore and offshore thermal events. These events are
434 now considered alongside the additional apatite U-Pb and compositional data we obtained, the
435 existing onshore thermochronology data and observations on the timing and magnitude of offshore
436 sedimentation. In doing this we show that thermochronology data from sedimentary basins can
437 reveal information on the sediment source region thermal history. Zircon fission-track, AFT and
438 Apatite (U-Th)/He data in the onshore region adjacent to the borehole (c.f. Fig. 1b) are shown in
439 SI-5. The regional thermochronology dataset for southern Africa and Namibia is shown and
440 discussed in detail in Wildman et al. (2019) and Krob et al. (2020), respectively.

441 Most of the samples in the borehole were deposited during the Early Cretaceous (c. 120 ± 20 Ma),
442 which overlaps with the syn-rift phase (145–125 Ma) and the beginning of the first post-rift event
443 in the mid- to Late Cretaceous (post-rift (i): 110–80 Ma). The AFT age components revealed from
444 mixture modelling, the t-T paths predicted by the thermal history model and the estimates of AFT
445 t_c all suggest that samples deposited during the syn-rift period contain a mixture of apatites that (i)
446 cooled slowly and resided at temperatures $<60^\circ\text{C}$ pre-rift, or (ii) cooled rapidly due to enhanced
447 rift-related erosion. The shift from a greater proportion of pre-rift cooling closure ages at greater
448 depth (e.g. from 2555 m [MT2363] to 2230 m [MT2359]) to a dominance of syn-rift closure times
449 in shallower samples (e.g. 2100 [MT2358] to 1410 m [MT2354]) (Fig. 8) is consistent with
450 continuous onshore erosion of the pre-rift surface that first removes rocks residing above or in
451 colder parts of the PAZ, and so have older AFT ages (Fig. 9a). These erosion products were then
452 transported and deposited in the basin. With the onset of rifting, enhanced erosion exhumes
453 material deeper in or hotter than the PAZ. This rapid cooling yielded apatites with syn-rift AFT
454 ages that were deposited in syn-rift sediments on top of the earlier sediments with older pre-rift
455 AFT ages in the offshore basin (Fig. 9b, c). Rapid denudation at the time of rifting has been
456 advocated along several passive margin settings driven by erosion in response to rapid base-level
457 fall and/or regional or local tectonic uplift (Gilchrist and Summerfield, 1990; van der Beek et al,
458 2002). Onshore AFT data along African margins and other passive margins globally have been
459 interpreted in terms of a rift-related increase in erosion rate (e.g. Wildman et al., 2015, 2016,
460 Gallagher et al, 1998, Gallagher and Brown 1997, 1999) (Fig. 10).

461 Apatite U-Pb ages from samples MT2354 to MT2363 (i.e. > -1410 m), are predominantly in the
462 range 650–450 Ma (i.e. Pan-African), with a median value of 528 Ma, and mean of 597 Ma.
463 Several grains from MT2359, show older, Neoproterozoic (c. 0.8–1 Ga) apatite U-Pb ages,
464 however in the other samples only sporadic grains yield ages that are Neoproterozoic or older.
465 Similarly, occasional grains, show younger ages contemporaneous with the deposition of the
466 Karoo Supergroup (i.e. Permian–Triassic). Regardless of the measured apatite U-Pb age or the
467 AFT age component to which single apatite grains belong to, the majority of grains plot in the
468 high-grade metamorphic rock field on the Sr/Y vs Σ LREE bivariate plot (Fig. 4d).

469 As discussed below, in the Namibian Damara Belt (Fig. 1a), the magnitude of post-rift erosion has
470 been large enough to remove any obvious record of the syn-rift event in AFT data from single
471 surface bedrock samples. However, recent modelling of a vertical profile of AFT and apatite (U-
472 Th)/He (AHe) data from the Brandberg Massif, has shown cooling between 130–100 Ma
473 (Margirier et al., 2019). Further north along the Kaoko Belt, Krob et al. (2020) present ZFT data
474 that yield ages of 310 to 430 Ma. AFT ages presented by Krob et al. (2020) range from c. 60–390
475 Ma, but many AFT ages are Early to mid-Cretaceous and are attributed to thermal resetting during
476 the emplacement of the Etendeka volcanics followed by protracted cooling. In addition to possible
477 magmatic heating these rocks may have subject to total annealing due to their pre-rifting depth in
478 the crust. They also resided below the section that recorded rapid syn-rift cooling, which was
479 eroded and deposited in the offshore (Fig. 7). Erosion at this time is also supported by sediment
480 volume estimates in the Orange and Walvis basins that suggest an influx of sediment at the time of
481 rifting (e.g. Rouby et al., 2009; Guillocheau et al., 2012; Baby et al., 2020) (Fig. 10).

482 Following syn-rift erosion and sedimentation, the inferred thermal history implies relative stability
483 until c. 90 Ma consistent with a reduction in tectonic activity following continental break-up (Fig.
484 7a). Estimates of sediment accumulation rates in the offshore basins varies, with the southern
485 Orange Basin having higher sedimentation accumulation rates than the Walvis Basin in the north
486 (Guillocheau et al., 2012). However, more recent work on sediment volumes in the Walvis Basin
487 by Baby et al. (2020) has predicted accumulated volumes remained relatively high during the mid-
488 Cretaceous (Fig. 10). It is possible that the borehole location did not experience burial-related
489 heating during this time because (i) there was a coincident decrease in heat flow, (ii) the total
490 amount of sediment deposited was too low to cause a recordable thermal effect or (iii) the
491 sediment bypassed the borehole and was deposited in more distal parts of the margin.

492 At 90 Ma, the data imply a period of rapid post-depositional heating, considered most likely to be
493 burial related (Fig. 9d). The timing of this agrees with the well-documented onshore mid-
494 Cretaceous cooling episode (c. 110–80 Ma) inferred from AFT and AHe data from along the
495 southwest (Kounov et al., 2009; Wildman et al., 2015, 2016), southern (Tinker et al., 2008b; Green
496 et al., 2016) and southeast (Brown et al., 2002) margins of southern Africa and across a large
497 section of the southwestern African plateau (Wildman et al., 2017; Stanley et al., 2013; Kounov et
498 al., 2013) (Fig. 10). The thermal histories for subsamples from 1120m and 870m depth show rapid
499 pre-depositional cooling just prior to deposition and yield t_c estimates of 101 ± 3 Ma and 95 ± 1 Ma,
500 respectively (Fig. 8). The onshore mid-Cretaceous cooling event has been interpreted as a result of
501 regional denudation and is supported by increased sedimentation rates and volumes in the offshore
502 Namibian and South African basins (Guillocheau et al., 2012; Tinker et al., 2008a; Baby et al.,
503 2020; Rouby et al., 2009) (Fig. 10).

504 Regional uplift and westward tilting caused by the African plate moving over a buoyant mantle
505 superplume has been suggested as a mechanism to explain the pattern and timing of onshore
506 erosion and offshore accumulation (Fig. 10) in the mid- to Late Cretaceous (c. 100–65 Ma) (Braun
507 et al., 2014). However, spatial variations in apatite thermochronology data and thermal histories
508 across structural lineaments along the margin and at the interior craton boundary suggests local
509 structural controls are also important (Raab et al. 2002; Kounov et al., 2009; Wildman et al. 2015,
510 2016, 2017). Despite the mid- to Late Cretaceous (c. 110–80 Ma) being the predominant cooling
511 signature onshore, it is largely absent from our thermal history, except for two sub-samples
512 showing pre-depositional cooling at this time. The limited record in the borehole samples of pre-
513 depositional cooling corresponding to the first post-rift event in the mid- to Late Cretaceous
514 ('post-rift (i)') (110–80 Ma) may be a consequence of later erosion, observed in the thermal
515 history as rapid cooling at 65–60 Ma (Fig. 7a), which removed the mid- to Late Cretaceous
516 sediments that contained this record (Fig. 9e). Additionally, subsidence of the distal margin and
517 uplift of the proximal part of the offshore region in the mid-Cretaceous (de Vera et al., 2010) may
518 have resulted in most of the sediments delivered to the Atlantic at that time accumulating further
519 oceanward than the location of the borehole.

520 The most significant post-depositional cooling episode occurs at c. 65–60 Ma. This timing is
521 dominant in the onshore cooling signal across the Damara Belt in north-western Namibia adjacent
522 to the basin where our borehole is located (Raab et al., 2002, 2005; Brown et al., 2014). Many of

523 the measured AFT ages onshore are in the range from 60 to 120 Ma, with Late Cretaceous AFT
524 ages forming a clear spatial relationship that matches the NE-SW trend of the Damara Belt and
525 extends c. 400 km inland on to the interior plateau (Fig. 2 in Raab et al., 2002). The surrounding
526 AFT ages are older than the timing of rifting and are commonly >300 Ma. Thermal modelling of
527 the AFT data implies rapid cooling began between 80–60 Ma in the Damara Belt and this has been
528 attributed to a post-rift event ('post-rift (ii)') involving local reactivation of NE-SW shear zones
529 (Fig. 1) in response to a change in plate motions (Raab et al., 2002; Brown et al., 2014).
530 Geophysical data show that the major Pan-African tectonic lineaments of the Damara Orogen
531 extend well into the offshore domain (Corner, 2000) and may have also experienced local
532 reactivation accompanied by denudation. A provenance signal with a record of onshore cooling at
533 this time is only observed for one age component in the shallowest sample, deposited just after this
534 cooling episode (Fig. 7a). This sample has two other age components with older estimated AFT t_c
535 values (130 Ma and 280 Ma) (Fig. 8). This suggests that, apart from areas of local reactivation, the
536 magnitude of onshore erosion was generally not enough to exhume and remove rocks from depths
537 in the crust that were hot enough (in or hotter than the PAZ) to have registered this Late
538 Cretaceous cooling event.

539 The two shallowest samples (MT2351 and MT2352) have age components of Late Palaeozoic,
540 Early Palaeozoic and Neoproterozoic t_c , respectively (Fig. 8). These timings are consistent with
541 the onshore AFT record observed inland of the escarpment and to the north and south of the
542 Damara Belt where measured AFT ages are >300 Ma. The presence of this signal offshore could
543 reflect a change to the drainage patterns, driven by structural reactivation and fault block uplift
544 that pushed erosion further inland than the escarpment, or by simply allowing erosion products
545 from further inland, with older AFT ages, to reach the offshore basin (Fig. 9e).

546 The change in provenance signal shown in the AFT data and in the pre-depositional thermal
547 history paths for the shallow samples (MT2351–MT2353) is reflected in a change in the pattern of
548 apatite U-Pb ages. In these samples, there is a greater amount of grains with Neoproterozoic U-Pb
549 apatite ages. A significant proportion of ages, particularly for MT2352, are Archean in age, which
550 supports our interpretation that onshore post-rift erosion moved inland and exhumed the
551 previously slowly eroding interior cratonic regions due to regional uplift and/or movement along
552 the faults along the Damara orogenic belt. Further support of this interpretation is provided by the
553 Sr/Y vs Σ LREE bivariate plot for MT2352 (Fig. 4e). This shows a significant cluster of datapoints

554 straddling the ultramafic/alkali-rich igneous fields of the plot, which correspond to the older single
555 grain AFT and U-Pb ages in MT2352 (Fig. 4b). The shallowest sample, MT2351, shows a far
556 more mixed apatite composition that does not correlate with the AFT age component to which the
557 apatites are assigned (Fig. 4f), and an absence of Archean U-Pb ages. This may indicate another
558 change to the source region from the interior craton to the younger (i.e. Neoproterozoic) basement
559 and Pan-African rocks that still outcrop onshore.

560 A late Eocene-Early Oligocene (c. 35–30 Ma) surface uplift event has been proposed based on
561 regional mapping of geomorphic planation surfaces, river profile analysis, and the identification of
562 a regional offshore erosional unconformity at this time. Interpreted planation surfaces are typically
563 low relief to flat, weathered surfaces, however, their preservation over geological timescales has
564 been questioned (Gilchrist and Summerfield, 1991; Phillips, 2002) and their use as markers for
565 landscape evolution debated in other settings (e.g. Green et al., 2013, Pedersen et al., 2016,
566 Egholm et al., 2017). Recent work has revised the identification and classification of African
567 planation surfaces and other geomorphic features (see Guillocheau et al., 2018; Dauteuil et al.,
568 2015; Picart et al., 2020). The prevailing climate conditions drives the erosion and/or weathering
569 process that formed a particular landform, while tectonic processes affect the geometry of the
570 surfaces. Quantitative dating of the formation and deformation of planar weathered surfaces
571 remains challenging (e.g. Vasconcelos and Carmo, 2018). More commonly, qualitative dating
572 relies on ascribing relative age ranges based on the vertical position and geometries of different
573 surfaces and their relationships to any available well-dated geological markers (e.g. Picart et al.,
574 2020). Based on the geometries of the surfaces Picart et al. (2020) conclude that a long-
575 wavelength bulging occurred during the Oligocene. This bulging is suggested to be a consequence
576 of spreading rate changes at the end of the Eocene. Surface uplift in the Oligocene is suggested to
577 be on the order of 400–500 m and has also been attributed to sea-level fall and small-scale
578 convection in the upper mantle causing tilting of the South Africa plateau (Baby et al., 2018). In
579 response to domal uplift, major rivers are predicted to deeply incise the planar surfaces and form
580 the present-day south African relief (Roberts and White, 2010). However, to be consistent with
581 regional thermochronological data, the total thickness of regional denudation must be < 1–1.5 km
582 (Wildman et al., 2015; Stanley et al., 2013).

583 The final cooling event inferred in the thermal history starting at c. 35 Ma and continuing to the
584 present day, is coincident with the timing of the Oligocene unconformity and surface uplift. The

585 thermal history does not show any additional structure that could be correlated with the minor
586 Miocene (c. 11 Ma) unconformity described by Baby et al. (2018). This unconformity is suggested
587 to be traceable across the entire SW African margin and is associated with a dramatic decrease in
588 continental siliciclastic supply (Baby et al., 2018). The thermal impact this event may simply have
589 been too small to be recorded in the data as the samples had already been exhumed to shallower
590 crustal depths and lower temperatures. The cooling history from c. 35 Ma to present-day could be
591 interpreted as a final phase of continuous denudation, which removed a thickness of about 800 m.
592 While the observed unconformities may imply some post-Oligocene erosion, our thermal history
593 would imply sub-aerial erosion in the basin right up to the present-day, which is not the case.
594 Moreover, the offshore record in the Walvis and Orange Basins during the Cenozoic is
595 characterised by low sediment volumes and limited deposition of siliciclastic material from the
596 onshore (Fig. 10) (Baby et al. 2020). Additionally, regional onshore erosion rates across Namibia
597 and southwestern African during the Cenozoic, revealed by AFT, AHe and cosmogenic nuclide
598 data, are typically <40 m/Myr (Cockburn et al., 2000; Bierman and Caffee, 2001; Margirier et al.,
599 2019). This is attributed to the prevailing arid climate (Pickford and Senut, 1999) and overall
600 stability of the plateau and relatively small amounts of Oligocene uplift (Baby et al. 2018).

601 The onset of aridification in the mid-Late Miocene (Pickford and Senut, 1999, Pickford et al.,
602 2014), initiation of the northward flowing cold Benguela current in the Early Oligocene or earlier,
603 leading to the formation of the Namib Desert (van Zinderen Bakker, 1975) and global drop in
604 ocean temperatures of c. 10-15°C from the mid-Eocene Climatic Optimum (~40 Ma) to Present
605 (Zachos et al., 2008) may have all contributed to the final cooling phase, with relatively little
606 denudation required (Fig. 9f). It is possible that the AFT data simply do not have the sensitivity to
607 identify specific thermal perturbations related to the minor Miocene erosion event and/or ocean
608 temperature and the inferred thermal history from 35 Ma to present-day represents a simplified
609 approximation of the most recent cooling experienced by the samples.

610 CONCLUSIONS

611 We have presented a suite of AFT data, acquired using both the EDM and LA-ICP-MS methods,
612 on 13 samples from a borehole from offshore Namibia. These data imply the samples have not
613 been hot enough post-deposition to remove all pre-deposition, or inherited, fission tracks. Using
614 Bayesian mixture modelling, we identified AFT age components in each sample, and assigned the

615 AFT data to their most probable age component to produce subsamples. We then obtained detailed
616 thermal history information using a multi-sample inversion approach, using these subsamples.
617 From the pre-depositional part of the thermal history we estimated a distribution of effective AFT
618 closure times for each subsample, and these were generally considerably older than the
619 stratigraphic ages.

620 This novel modelling approach allowed us to recover a record of onshore erosion and offshore
621 sedimentation from a single borehole profile. We identify rapid onshore exhumation at the time of
622 rifting and during the mid-Cretaceous, which is not observed in the onshore Namibian AFT data
623 due to the current level of rock exposure. We also identify a major heating and cooling episode in
624 the late Cretaceous followed by minor heating and cooling of the profile during the Cenozoic. The
625 post-rift events are attributed to regional tectonic and mantle processes. However, the inferred
626 thermal history over the Cenozoic may also reflect climatic and ocean temperature changes. By
627 combining our LA-ICP-MS fission track data and thermal history paths with REE composition
628 and U-Pb data we make inferences regarding the variations in the sediment sources and reveal
629 mid-late Cretaceous post-rift tectonics drove erosion several 100s of km inland. This demonstrates
630 the potential of the LA-ICP-MS fission track approach in detrital studies. It enables users to
631 rapidly acquire an AFT age, FT length information, compositional data and a U-Pb age from all
632 single grain and thus resolve the thermal history of the grain.

633 The inverse thermal history modelling approach was formulated to resolve pre- and post-
634 depositional thermal parts of the thermal history. This was possible because the magnitude of the
635 post-depositional heating was not sufficient to erase provenance-related thermal history signals.
636 Clearly there will be many cases where this is not the case, but then higher temperature sensitivity
637 thermochronometers (e.g. ZFT or zircon (U-Th)/He) may be of use. Thermochronometers
638 sensitive to lower temperatures (AHe, $^4\text{He}/^3\text{He}$) would also better constrain the more recent
639 cooling history if all factors causing age dispersion are constrained. Taken together, appropriately
640 selected offshore and onshore thermochronometric datasets should then provide a more integrated
641 and comprehensive source-to-sink evolution model for passive margins.

642

643 **ACKNOWLEDGEMENTS**

644 We would like to thank Canadian Natural Resources Ltd. for granting permission to publish the
645 data. We would also like to thank Nathan Cogné for his comments on an earlier version of this
646 work. This project has received funding from the European Union's Horizon 2020 research and
647 innovation programme under the Marie Skłodowska-Curie grant agreement No. 706976. DC
648 acknowledges support by a research grant from Science Foundation Ireland under Grant Number
649 13/RC/2092, which is co-funded under the European Regional Development Fund and by PIPCO
650 RSG and its member companies. We are grateful to Eva Enkelmann, Frank Lisker and an
651 anonymous reviewer for their comments on this manuscript and Nadine McQuarrie for editorial
652 handling.

653

654 **DATA AVAILABILITY STATEMENT**

655 Data available in article supplementary material

REFERENCES

- Amidon, W. H., Roden-Tice, M., Anderson, A. J., McKeon, R. E., & Shuster, D. L. (2016). Late Cretaceous unroofing of the White Mountains, New Hampshire, USA: An episode of passive margin rejuvenation?. *Geology*, 44(6), 415-418.
- Baby, G., Guillocheau, F., Braun, J., Robin, C., & Dall'Asta, M. (2020). Solid sedimentation rates history of the Southern African continental margins: Implications for the uplift history of the South African Plateau. *Terra Nova*, 32(1), 53-65.
- Baby, G., Guillocheau, F., Morin, J., Ressouche, J., Robin, C., Broucke, O., & Dall'Asta, M. (2018). Post-rift stratigraphic evolution of the Atlantic margin of Namibia and South Africa: Implications for the vertical movements of the margin and the uplift history of the South African Plateau. *Marine and Petroleum Geology*, 97, 169-191.
- Barbarand, J., Carter, A., Wood, I., & Hurford, T. (2003). Compositional and structural control of fission-track annealing in apatite. *Chemical Geology*, 198(1-2), 107-137.
- Bernet, M. (2009). A field-based estimate of the zircon fission-track closure temperature. *Chemical Geology*, 259(3-4), 181-189.
- Bernet, M., & Garver, J. I. (2005). Fission-track analysis of detrital zircon. *Reviews in Mineralogy and Geochemistry*, 58(1), 205-237.
- Bierman, P. R., & Caffee, M. (2001). Slow rates of rock surface erosion and sediment production across the Namib Desert and escarpment, southern Africa. *American Journal of Science*, 301(4-5), 326-358.
- Braun, J., Guillocheau, F., Robin, C., Baby, G., & Jelsma, H. (2014). Rapid erosion of the Southern African Plateau as it climbs over a mantle superswell. *Journal of Geophysical Research: Solid Earth*, 119(7), 6093-6112.
- Brown, R. W., Summerfield, M. A., & Gleadow, A. J. (2002). Denudational history along a transect across the Drakensberg Escarpment of southern Africa derived from apatite fission track thermochronology. *Journal of Geophysical Research: Solid Earth*, 107(B12), ETG-10.

Brown, R., Summerfield, M., Gleadow, A., Gallagher, K., Carter, A., Beucher, R., & Wildman, M. (2014). Intracontinental deformation in southern Africa during the Late Cretaceous. *Journal of African Earth Sciences*, 100, 20-41.

Carter, A. & Gallagher, K. 2004. Characterising the significance of provenance on the inference of thermal history models from apatite fission track data – A synthetic data study. In: *Detrital thermochronology – Provenance analysis, exhumation, and landscape evolution of mountain belts*. (Editors: Bernet, M. & Spiegel, C.). GSA Special Paper 378, 7-23.

Cherniak, D. J., & Watson, E. B. (2001). Pb diffusion in zircon. *Chemical Geology*, 172(1-2), 5-24.

Chew, D. M., & Donelick, R. A. (2012). Combined apatite fission track and U-Pb dating by LA-ICP-MS and its application in apatite provenance analysis. *Quantitative Mineralogy and Microanalysis of Sediments and Sedimentary Rocks: Mineralogical Association of Canada, Short Course*, 42, 219-247.

Chew, D. M., Donelick, R. A., Donelick, M. B., Kamber, B. S., & Stock, M. J. (2014a). Apatite chlorine concentration measurements by LA-ICP-MS. *Geostandards and Geoanalytical Research*, 38(1), 23-35.

Chew, D.M., Petrus, J.A. & Kamber, B.S. (2014b). U–Pb LA-ICPMS dating using accessory mineral standards with variable common Pb. *Chemical Geology*, 363, 185–199.

Clemson, J., Cartwright, J., & Booth, J. (1997). Structural segmentation and the influence of basement structure on the Namibian passive margin. *Journal of the Geological Society*, 154(3), 477-482.

Clemson, J., Cartwright, J., & Swart, R. (1999). The Namib Rift: a rift system of possible Karoo age, offshore Namibia. *Geological Society, London, Special Publications*, 153(1), 381-402.

Clift, P. D., Carter, A., & Hurford, A. J. (1996). Constraints on the evolution of the East Greenland Margin: Evidence from detrital apatite in offshore sediments. *Geology*, 24(11), 1013-1016.

Cockburn, H. A. P., Brown, R. W., Summerfield, M. A., & Seidl, M. A. (2000). Quantifying passive margin denudation and landscape development using a combined fission-track

thermochronology and cosmogenic isotope analysis approach. *Earth and Planetary Science Letters*, 179(3-4), 429-435.

Cogné, N., Chew, D. M., Donelick, R. A., & Ansberque, C. (2020). LA-ICP-MS apatite fission track dating: A practical zeta-based approach. *Chemical Geology*, 531, 119302.

Cogné, N., Gallagher, K., & Cobbold, P. R. (2011). Post-rift reactivation of the onshore margin of southeast Brazil: evidence from apatite (U–Th)/He and fission-track data. *Earth and Planetary Science Letters*, 309(1-2), 118-130.

Corner, B. (2000). Crustal framework of Namibia derived from magnetic and gravity data. *Communications of the Geological Survey of Namibia*, 12, 13-19.

Crowley, K.D. (1993), LENMODEL: A forward model for calculating length distributions and fission-track ages in apatite, *Comp. Geosci.* 19, 619-626

Dauteuil, O., Bessin, P., & Guillocheau, F. (2015). Cenozoic growth of the southern Africa landscape around the Orange Valley: a planation record of deformation and climate changes. *Geomorphology*, 233, 5-19.

De Vera, J., Granado, P., & McClay, K. (2010). Structural evolution of the Orange Basin gravity-driven system, offshore Namibia. *Marine and Petroleum Geology*, 27(1), 223-237.

Egholm, David L., John D. Jansen, Christian F. Brødstrup, Vivi K. Pedersen, Jane L. Andersen, Sofie V. Ugelvig, Nicolaj K. Larsen, and Mads F. Knudsen. "Formation of plateau landscapes on glaciated continental margins." *Nature Geoscience* 10, no. 8 (2017): 592-597.

Frimmel, H. E. (1995). Metamorphic evolution of the Gariiep Belt. *South African Journal of Geology*, 98(2), 176-190.

Gallagher, K. (2012). Transdimensional inverse thermal history modeling for quantitative thermochronology. *Journal of Geophysical Research: Solid Earth*, 117(B2).

Gallagher, K., & Brown, R. (1997). The onshore record of passive margin evolution. *Journal of the Geological Society*, 154(3), 451-457.

Gallagher, K., & Brown, R. (1999). Denudation and uplift at passive margins: the record on the Atlantic Margin of southern Africa. *Philosophical Transactions of the Royal Society of London. Series A: Mathematical, Physical and Engineering Sciences*, 357(1753), 835-859.

Gallagher, K., Brown, R., & Johnson, C. (1998). Fission track analysis and its applications to geological problems. *Annual Review of Earth and Planetary Sciences*, 26(1), 519-572.

Gallagher, K., Stephenson, J., Brown, R., Holmes, C., & Fitzgerald, P. (2005). Low temperature thermochronology and modeling strategies for multiple samples 1: Vertical profiles. *Earth and Planetary Science Letters*, 237(1-2), 193-208.

Gibson, S. A., Thompson, R. N., & Day, J. A. (2006). Timescales and mechanisms of plume–lithosphere interactions: $^{40}\text{Ar}/^{39}\text{Ar}$ geochronology and geochemistry of alkaline igneous rocks from the Paraná–Etendeka large igneous province. *Earth and Planetary Science Letters*, 251(1-2), 1-17.

Gilchrist, A. R., & Summerfield, M. A. (1990). Differential denudation and flexural isostasy in formation of rifted-margin upwarps. *Nature*, 346(6286), 739-742.

Gilchrist, A. R., & Summerfield, M. A. (1991). Denudation, isostasy and landscape evolution. *Earth Surface Processes and Landforms*, 16(6), 555-562.

Green, P. F., Duddy, I. R., Japsen, P., Bonow, J. M., & Malan, J. A. (2017). Post-breakup burial and exhumation of the southern margin of Africa. *Basin Research*, 29(1), 96-127.

Green, P. F., Lidmar-Bergström, K., Japsen, P., Bonow, J. M., & Chalmers, J. A. (2013). Stratigraphic landscape analysis, thermochronology and the episodic development of elevated, passive continental margins. *Geological Survey of Denmark & Greenland Bulletin*, (30).

Guillocheau, F., Rouby, D., Robin, C., Helm, C., Rolland, N., De Veslud, C. L. C., & Braun, J. (2012). Quantification and causes of the terrigenous sediment budget at the scale of a continental margin: a new method applied to the Namibia–South Africa margin. *Basin Research*, 24(1), 3-30.

Guillocheau, F., Simon, B., Baby, G., Bessin, P., Robin, C., & Dauteuil, O. (2018). Planation surfaces as a record of mantle dynamics: the case example of Africa. *Gondwana Research*, 53, 82-98.

Helland-Hansen, W., Sømme, T. O., Martinsen, O. J., Lunt, I., & Thurmond, J. (2016). Deciphering Earth's natural hourglasses: perspectives on source-to-sink analysis. *Journal of Sedimentary Research*, 86(9), 1008-1033.

Hoernle, K., Rohde, J., Hauff, F., Garbe-Schönberg, D., Homrighausen, S., Werner, R., & Morgan, J. P. (2015). How and when plume zonation appeared during the 132 Myr evolution of the Tristan Hotspot. *Nature Communications*, 6(1), 1-10.

Holtar, E., and A. W. Forsberg, 2000, Postrift development of the Walvis Basin, Namibia: results from the exploration campaign in Quadrant 1911, in M. R. Mello and B. J. Katz, eds., *Petroleum systems of South Atlantic margins: AAPG Memoir 73*, p. 429–446

Holzförster, F., Stollhofen, H., & Stanistreet, I. G. (1999). Lithostratigraphy and depositional environments in the Waterberg-Erongo area, central Namibia, and correlation with the main Karoo Basin, South Africa. *Journal of African Earth Sciences*, 29(1), 105-123.

Homke, S., Vergés, J., Van Der Beek, P., Fernández, M., Saura, E., Barbero, L., ... & Labrin, E. (2010). Insights in the exhumation history of the NW Zagros from bedrock and detrital apatite fission-track analysis: evidence for a long-lived orogeny. *Basin Research*, 22(5), 659-680.

Hurford AJ (1986) Cooling and uplift patterns in the Lepontine Alps South Central Switzerland and an age of vertical movement on the Insubric fault line. *Contrib Mineral Petrol* 92:413–427

Hurford, A. J., & Green, P. F. (1983). The zeta age calibration of fission-track dating. *Chemical Geology*, 41, 285-317.

Jasra, A., Stephens, D. A., Gallagher, K., & Holmes, C. C. (2006). Bayesian mixture modelling in geochronology via Markov chain Monte Carlo. *Mathematical Geology*, 38(3), 269-300.

Jung, S., Brandt, S., Bast, R., Scherer, E. E., & Berndt, J. (2019). Metamorphic petrology of a high-T/low-P granulite terrane (Damara belt, Namibia)—Constraints from pseudosection modelling and high-precision Lu–Hf garnet-whole rock dating. *Journal of Metamorphic Geology*, 37(1), 41-69.

Jung, S., Hauff, F., & Berndt, J. (2020). Generation of a potassic to ultrapotassic alkaline complex in a syn-collisional setting through flat subduction: Constraints on magma sources and processes (Otjimbingwe alkaline complex, Damara orogen, Namibia). *Gondwana Research*, 82, 267-287.

Ketcham, R. A., Carter, A., Donelick, R. A., Barbarand, J., & Hurford, A. J. (2007). Improved modeling of fission-track annealing in apatite. *American Mineralogist*, 92(5-6), 799-810.

Kounov, A., Viola, G., De Wit, M., & Andreoli, M. A. G. (2009). Denudation along the Atlantic passive margin: new insights from apatite fission-track analysis on the western coast of South Africa. *Geological Society, London, Special Publications*, 324(1), 287-306.

Kounov, A., Viola, G., Dunkl, I., & Frimmel, H. E. (2013). Southern African perspectives on the long-term morpho-tectonic evolution of cratonic interiors. *Tectonophysics*, 601, 177-191.

Krob, F. C., Eldracher, D. P., Glasmacher, U. A., Husch, S., Salomon, E., Hackspacher, P. C., & Titus, N. P. (2020). Late Neoproterozoic-to-recent long-term t–T-evolution of the Kaoko and Damara belts in NW Namibia. *International Journal of Earth Sciences*, 109(2), 537-567.

Kroner, S., Konopásek, J., Kroner, A., Passchier, C. W., Poller, U., Wingate, M. T. D., & Hofmann, K. H. (2004). U-Pb and Pb-Pb zircon ages for metamorphic rocks in the Kaoko Belt of Northwestern Namibia: A Palaeo-to Mesoproterozoic basement reworked during the Pan-African orogeny. *South African Journal of Geology*, 107(3), 455-476.

Ksienzyk, A. K., Dunkl, I., Jacobs, J., Fossen, H., & Kohlmann, F. (2014). From orogen to passive margin: constraints from fission track and (U–Th)/He analyses on Mesozoic uplift and fault reactivation in SW Norway. *Geological Society, London, Special Publications*, 390(1), 679-702.

Lee, J. K., Williams, I. S., & Ellis, D. J. (1997). Pb, U and Th diffusion in natural zircon. *Nature*, 390(6656), 159-162.

Leturmy, P., Lucazeau, F., & Brigaud, F. (2003). Dynamic interactions between the Gulf of Guinea passive margin and the Congo River drainage basin: 1. Morphology and mass balance. *Journal of Geophysical Research: Solid Earth*, 108(B8).

Light, M. P. R., Maslanyj, M. P., Greenwood, R. J., & Banks, N. L. (1993). Seismic sequence stratigraphy and tectonics offshore Namibia. Geological Society, London, Special Publications, 71(1), 163-191.

Malusà, M. G., & Fitzgerald, P. G. (Eds.). (2019). Fission-track thermochronology and its application to geology. Springer International Publishing.

Margirier, A., Braun, J., Gautheron, C., Carcaillet, J., Schwartz, S., Jamme, R. P., & Stanley, J. (2019). Climate control on Early Cenozoic denudation of the Namibian margin as deduced from new thermochronological constraints. *Earth and Planetary Science Letters*, 527, 115779.

Marsh, J. S. (2010). The geochemistry and evolution of Palaeogene phonolites, central Namibia. *Lithos*, 117(1-4), 149-160.

Miller, R. M. (1979). The Okahandja lineament, a fundamental tectonic boundary in the Damara Orogen of South West Africa/Namibia. *South African Journal of Geology*, 82(3), 349-362.

Miller, R. M. (1983). The Pan-African Damara Orogen of South West Africa/Namibia. In *Evolution of the Damara Orogen of South West Africa/Namibia*.

Moore, M. E., Gleadow, A. J., & Lovering, J. F. (1986). Thermal evolution of rifted continental margins: new evidence from fission tracks in basement apatites from southeastern Australia. *Earth and Planetary Science Letters*, 78(2-3), 255-270.

O'Connor, J. M., Jokat, W., Le Roex, A. P., Class, C., Wijbrans, J. R., Keßling, S., Kuiper, K. F., & Nebel, O. (2012). Hotspot trails in the South Atlantic controlled by plume and plate tectonic processes. *Nature Geoscience*, 5(10), 735-738.

O'Sullivan, G., Chew, D., Kenny, G., Henrichs, I., & Mulligan, D. (2020). The trace element composition of apatite and its application to detrital provenance studies. *Earth-Science Reviews*, 201, 103044.

Passchier, C. W., Trouw, R. A. J., Ribeiro, A., & Paciullo, F. V. P. (2002). Tectonic evolution of the southern Kaoko belt, Namibia. *Journal of African Earth Sciences*, 35(1), 61-75.

Pedersen, V. K., Huisman, R. S., & Moucha, R. (2016). Isostatic and dynamic support of high topography on a North Atlantic passive margin. *Earth and Planetary Science Letters*, 446, 1-9.

Phillips J D, 2002. Erosion, isostatic response, and the missing peneplains. *Geomorphology* 45, 225–241.

Picart, C., Dauteuil, O., Pickford, M., & Owono, F. M. (2020). Cenozoic deformation of the South African plateau, Namibia: Insights from planation surfaces. *Geomorphology*, 350, 106922.

Pickford, M., & Senut, B. (1999). Geology and palaeobiology of the Namib desert Southwest Africa. Geological Survey of Namibia, Memoir, 18, 155.

Pickford, M., Senut, B., Mocke, H., Mourer-Chauviré, C., Rage, J. C., & Mein, P. (2014). Eocene aridity in southwestern Africa: timing of onset and biological consequences. *Transactions of the Royal Society of South Africa*, 69(3), 139-144.

Raab, M. J., Brown, R. W., Gallagher, K., Carter, A., & Weber, K. (2002). Late Cretaceous reactivation of major crustal shear zones in northern Namibia: constraints from apatite fission track analysis. *Tectonophysics*, 349(1-4), 75-92.

Raab, M. J., Brown, R. W., Gallagher, K., Weber, K., & Gleadow, A. J. W. (2005). Denudational and thermal history of the Early Cretaceous Brandberg and Okenyenya igneous complexes on Namibia's Atlantic passive margin. *Tectonics*, 24(3).

Roberts, G. G., & White, N. (2010). Estimating uplift rate histories from river profiles using African examples. *Journal of Geophysical Research: Solid Earth*, 115(B2).

Rouby, D., Bonnet, S., Guillocheau, F., Gallagher, K., Robin, C., Biancotto, F., Dauteuil, O. & Braun, J. (2009). Sediment supply to the Orange sedimentary system over the last 150 My: An evaluation from sedimentation/denudation balance. *Marine and Petroleum Geology*, 26(6), 782-794.

Salazar-Mora, C. A., Huisman, R. S., Fossen, H., & Egydio-Silva, M. (2018). The Wilson cycle and effects of tectonic structural inheritance on rifted passive margin formation. *Tectonics*, 37(9), 3085-3101.

Seiler C, Kohn B, Gleadow A (2014) Apatite fission track analysis by LA-ICP-MS: an evaluation of the absolute dating approach. In: 14th International conference on thermochronology, Chamonix, September 2014, pp 11–12

Stanley, J. R., Flowers, R. M., & Bell, D. R. (2013). Kimberlite (U-Th)/He dating links surface erosion with lithospheric heating, thinning, and metasomatism in the southern African Plateau. *Geology*, 41(12), 1243-1246.

Tankard, A.J., Jackson, M., Eriksson, K.A., Hobday, D.K., Hunter, D.R., and Minter, W.E.L (1982), *Crustal Evolution of Southern Africa 3.8 Billion Years of Earth History*, Springer-Verlag Berlin Heidelberg, p. 523, ISBN: 978-1-4613-8149-5

Tinker, J., de Wit, M., & Brown, R. (2008a). Linking source and sink: evaluating the balance between onshore erosion and offshore sediment accumulation since Gondwana break-up, South Africa. *Tectonophysics*, 455(1-4), 94-103.

Tinker, J., de Wit, M., & Brown, R. (2008b). Mesozoic exhumation of the southern Cape, South Africa, quantified using apatite fission track thermochronology. *Tectonophysics*, 455(1-4), 77-93.

van der Beek, P., Robert, X., Mugnier, J. L., Bernet, M., Huyghe, P., & Labrin, E. (2006). Late Miocene–recent exhumation of the central Himalaya and recycling in the foreland basin assessed by apatite fission-track thermochronology of Siwalik sediments, Nepal. *Basin Research*, 18(4), 413-434.

van der Beek, P., Summerfield, M. A., Braun, J., Brown, R. W., & Fleming, A. (2002). Modeling postbreakup landscape development and denudational history across the southeast African (Drakensberg Escarpment) margin. *Journal of Geophysical Research: Solid Earth*, 107(B12), ETG-11.

van Zinderen Bakker, E. M. (1975). The origin and palaeoenvironment of the Namib Desert biome. *Journal of Biogeography*, 65-73.

Vasconcelos, P. M., & Carmo, I. D. O. (2018). Calibrating denudation chronology through $^{40}\text{Ar}/^{39}\text{Ar}$ weathering geochronology. *Earth-Science Reviews*, 179, 411-435.

Vermeesch, P. (2018). IsoplotR: A free and open toolbox for geochronology. *Geoscience Frontiers*, 9(5), 1479-1493.

Wanke, H., & Wanke, A. (2007). Lithostratigraphy of the Kalahari Group in northeastern Namibia. *Journal of African Earth Sciences*, 48(5), 314-328.

Ward, J. D. (1988). Eolian, fluvial and pan (playa) facies of the Tertiary Tsondab Sandstone Formation in the central Namib Desert, Namibia. *Sedimentary Geology*, 55(1-2), 143-162.

Ward, J. D., & Martin, H. (1987). A terrestrial conglomerate of Cretaceous age-A new record from the Skeleton Coast, Namib Desert. *Commun. Geol. Survey South West Africa/Namibia*, 3, 57-58.

Whitchurch, A. L., Carter, A., Sinclair, H. D., Duller, R. A., Whittaker, A. C., & Allen, P. A. (2011). Sediment routing system evolution within a diachronously uplifting orogen: Insights from detrital zircon thermochronological analyses from the South-Central Pyrenees. *American Journal of Science*, 311(5), 442-482.

Wildman, M., Brown, R., Beucher, R., Persano, C., Stuart, F., Gallagher, K., Schwanethal, J., & Carter, A. (2016). The chronology and tectonic style of landscape evolution along the elevated Atlantic continental margin of South Africa resolved by joint apatite fission track and (U-Th-Sm)/He thermochronology. *Tectonics*, 35(3), 511-545.

Wildman, M., Brown, R., Persano, C., Beucher, R., Stuart, F. M., Mackintosh, V., Gallagher, K., Schwanethal, J., & Carter, A. (2017). Contrasting Mesozoic evolution across the boundary between on and off craton regions of the South African plateau inferred from apatite fission track and (U-Th-Sm)/He thermochronology. *Journal of Geophysical Research: Solid Earth*, 122(2), 1517-1547.

Wildman, M., Brown, R., Watkins, R., Carter, A., Gleadow, A., & Summerfield, M. (2015). Post break-up tectonic inversion across the southwestern cape of South Africa: New insights from apatite and zircon fission track thermochronometry. *Tectonophysics*, 654, 30-55.

Will, T. M., & Frimmel, H. E. (2018). Where does a continent prefer to break up? Some lessons from the South Atlantic margins. *Gondwana Research*, 53, 9-19.

Zachos, J. C., Dickens, G. R., & Zeebe, R. E. (2008). An early Cenozoic perspective on greenhouse warming and carbon-cycle dynamics. *Nature*, 451(7176), 279-283

Sample	Strat. Age	Depth (m)	N_s	N_i^*	$P(\chi^2)$	Disp.	C. AFT Age	#Xtls	MTL	SD	Proj. MTL	SD	#CT	Dpar	SD
MT2351	50 ± 20	650	3325	6464	0.00	47%	117.9 ± 7.9	58	12.56 ± 0.13	1.90	13.74 ± 0.09	1.34	214	1.95 ± 0.02	0.35
MT2352	80 ± 15	870	6727	5472	0.00	82%	317 ± 33	63	12.31 ± 0.09	1.78	13.55 ± 0.06	1.27	430	2.20 ± 0.02	0.41
MT2353	80 ± 15	1120	2111	5224	0.00	37%	94.2 ± 6.2	39	12.70 ± 0.11	1.31	13.82 ± 0.08	0.96	153	1.79 ± 0.02	0.27
MT2354	120 ± 20	1410	5397	13580	0.00	39%	93.5 ± 4.9	65	12.37 ± 0.09	1.48	13.57 ± 0.06	1.00	255	1.99 ± 0.02	0.25
MT2355	120 ± 20	1650	4862	11890	0.00	26%	90.2 ± 3.5	63	12.17 ± 0.11	1.58	13.44 ± 0.07	1.07	207	1.93 ± 0.01	0.28
MT2356	120 ± 20	1775	4592	10882	0.00	31%	92.4 ± 4	63	11.81 ± 0.08	1.35	13.16 ± 0.06	0.96	263	1.75 ± 0.01	0.25
MT2357	120 ± 20	1900	8294	18220	0.00	23%	96.8 ± 3.1	69	11.46 ± 0.06	1.42	12.96 ± 0.04	0.96	515	1.85 ± 0.01	0.25
MT2358	120 ± 20	2100	5472	12851	0.00	29%	94.6 ± 3.9	61	11.48 ± 0.09	1.52	12.96 ± 0.06	1.05	271	1.81 ± 0.01	0.24
MT2359	120 ± 20	2230	3593	7835	0.00	39%	102.4 ± 6.5	43	11.11 ± 0.11	1.65	12.69 ± 0.07	1.04	219	1.77 ± 0.01	0.20
MT2360	120 ± 20	2275	6789	13963	0.00	41%	108.8 ± 6	63	11.05 ± 0.10	1.73	12.66 ± 0.06	1.08	311	1.93 ± 0.01	0.24
MT2361	120 ± 20	2350	9436	20089	0.00	35%	108 ± 4.9	66	10.80 ± 0.08	1.67	12.53 ± 0.05	1.03	459	1.93 ± 0.01	0.25
MT2362	120 ± 20	2460	8980	17808	0.00	42%	104.6 ± 5.8	62	10.66 ± 0.08	1.56	12.37 ± 0.05	1.02	418	1.77 ± 0.01	0.21
MT2363	120 ± 20	2555	1829	4442	0.00	58%	111 ± 11	38	10.45 ± 0.18	1.94	12.29 ± 0.11	1.17	118	1.72 ± 0.01	0.22

Table 1: Summary of AFT data (composite AFT-90 + LA-ICP-MS AFT data. See SI-Table 1 and SI-Table 2 for summary data of AFT-90 and LA-ICP-MS AFT datasets. N_s = Total number of spontaneous tracks. N_i = Total number of induced tracks. *The total number of N_i is the sum of the N_i counted in the AFT-90 EDM dataset and the N_i determined for each grain dated using LA-ICP-MS based on the measured LA-ICP-MS AFT age, its error and the zeta calibration factor, ρ_d and N_d (track density and number of tracks counted for the U dosimeter) from the AFT-90 EDM analyses. $P(\chi^2)$ is the chi-squared test for population homogeneity. Disp. = the single grain age dispersion. C. AFT Age = central AFT age and 1σ standard error. #Xtls = total number of crystals dated (AFT-90 and LA-ICP-MS data combined). MTL = mean track length (measured in the LA-ICP-MS AFT samples only) and 1σ standard error. Proj. MTL = mean track length corrected for c-axis orientation and 1σ standard error. #CT = number of confined track lengths measured in both LA-ICP-MS and AFT-90 EDM datasets. D_{par} = mean etch pit size and 1σ standard error. SD = standard deviation on length measurements.

Group	Pre-depositional cooling	Subsample	Stratigraphic Age	
I	Protracted cooling initiated prior to 150 Ma	MT2363-1	120 ± 20 Ma	
		MT2362-2		
		MT2361-2		
		MT2360-2		
		MT2359-2		
		MT2356-3		
		MT2352-3	80 ± 15 Ma	
		MT2352-2		
		MT2351-3	50 ± 15 Ma	
II	Rapid cooling across the base of the Partial Annealing Zone (PAZ) between 145–125 Ma	MT2362-1	120 ± 20 Ma	
		MT2361-1		
		MT2360-2		
		MT2359-1		
		MT2358-1		
		MT2357-1		
		MT2356-2		
		MT2356-1		
		MT2355-1		
		MT2354-1		
		MT2351-2	50 ± 15 Ma	
III	Rapid Late Cretaceous cooling initiating at:	100 - 90 Ma	MT2353-1	80 ± 15 Ma
			MT2352-1	
		70 Ma	MT2351-1	

Table 2: Summary of pre-depositional thermal history for each subsample. See SI-4 for an illustration of the thermal history split into the three groups.

Supplementary Table 1: Summary data table for AFT analysis collected using the external detector method (i.e. AFT-90 dataset).

Supplementary Table 2: Summary data table for LA-ICP-MS AFT analysis.

Supplementary Table 3: Single-grain LA-ICP-MS AFT data, apatite U-Pb data and apatite composition.

Supplementary Table 4: Summary AFT data for individual subsamples

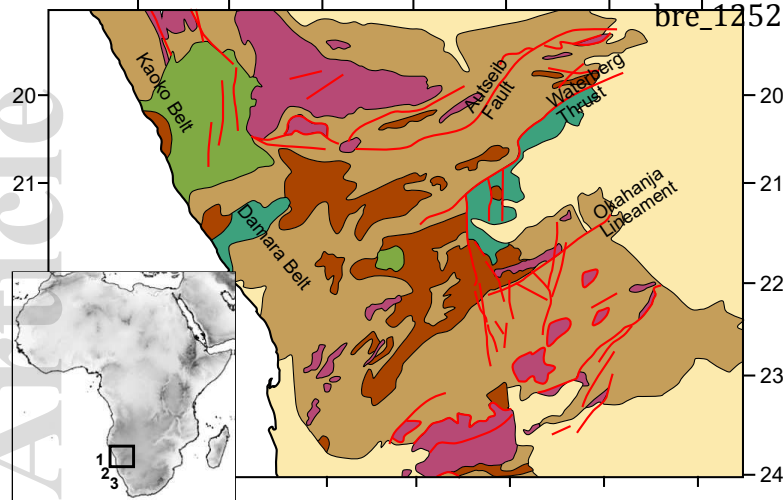
Supplementary Information 1: Track length distribution histograms.

**Supplementary Information 2: Radial plots of single grain age showing relationship with Dpar and Cl wt%.
Plot of Dpar vs. Cl wt%.**

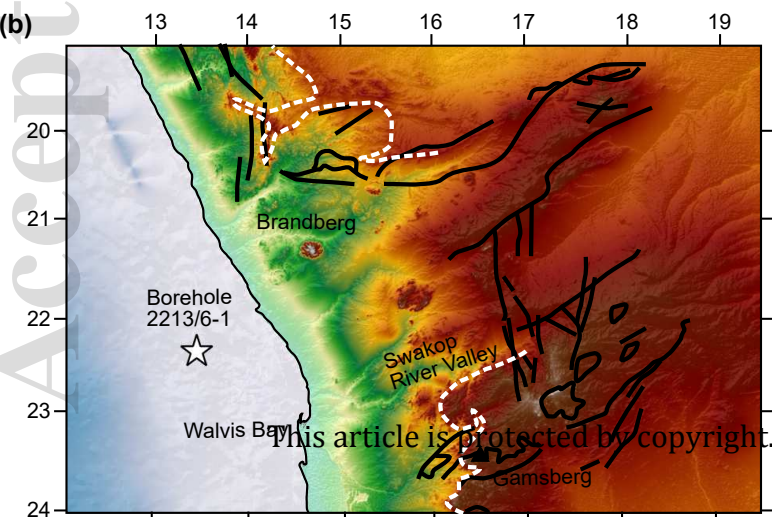
Supplementary Information 3: Distributions of the inferred pre-depositional time-temperature points.

Supplementary Information 4: Full expected thermal history model and thermal history paths colour coded to reflect pre-depositional group (cf. Table 2 in main text).

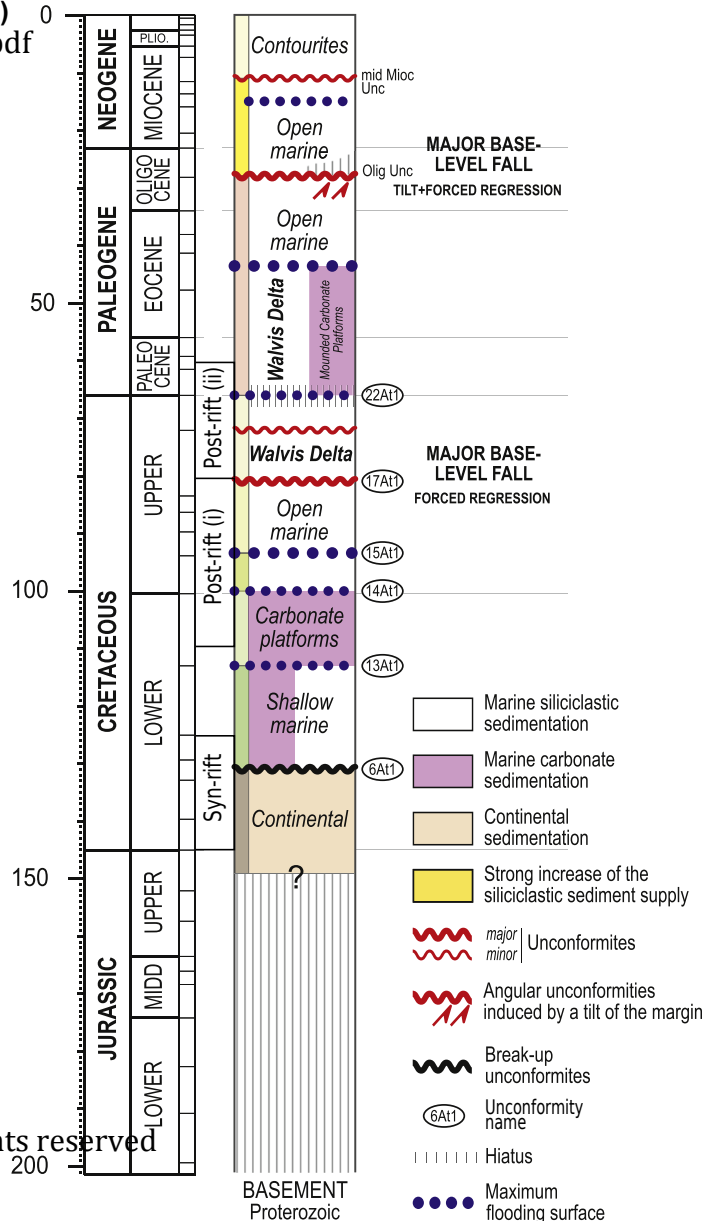
Supplementary Information 5: Location and age range of onshore ZFT, AFT and Apatite (U-Th)/He data adjacent to the location of Borehole 2213/6-1 (c.f. Fig. 1b).



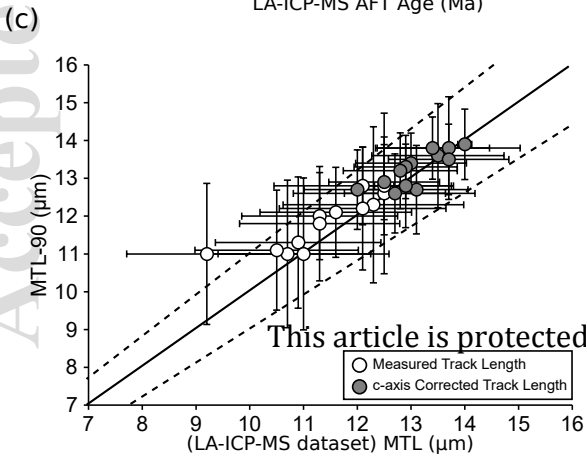
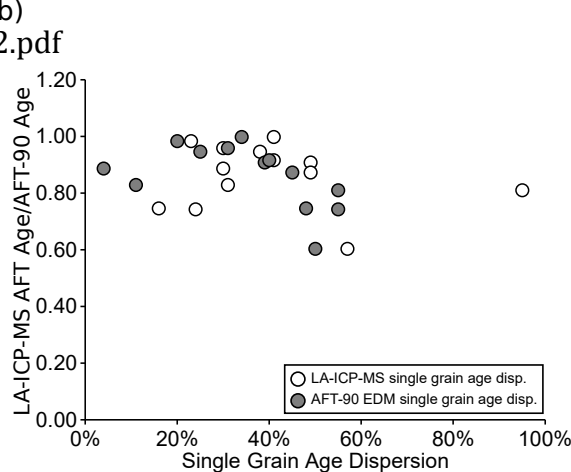
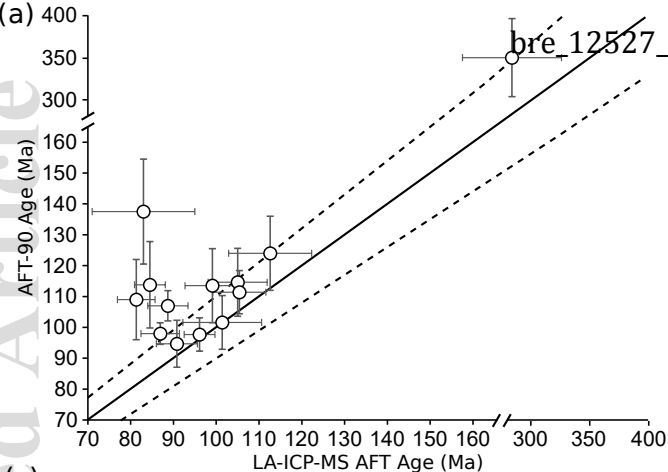
- Offshore Basins:
- 1 - Walvis Basin
 - 2 - Luderitz Basin
 - 3 - Orange Basin
- Cenozoic Cover Sediments
 - Early Cretaceous Etendeka Lavas
 - Permian-Triassic Karoo Supergroup
 - Neoproterozoic - Cambrian Nama Group
 - Neoproterozoic Damara Supergroup
 - Archean - Proterozoic Basement
 - Basement Faults



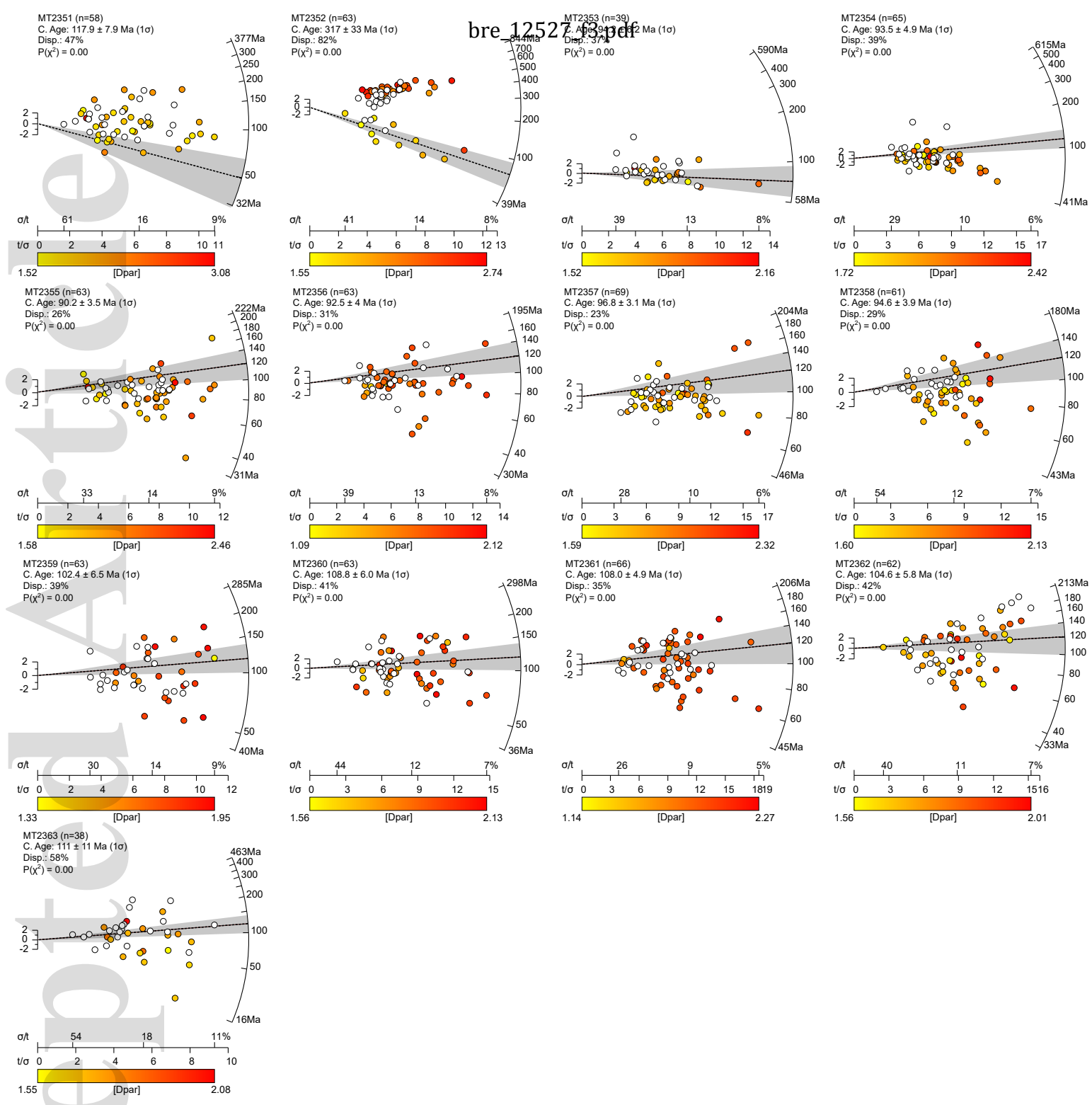
----- Top of Escarpment ——— Basement Faults

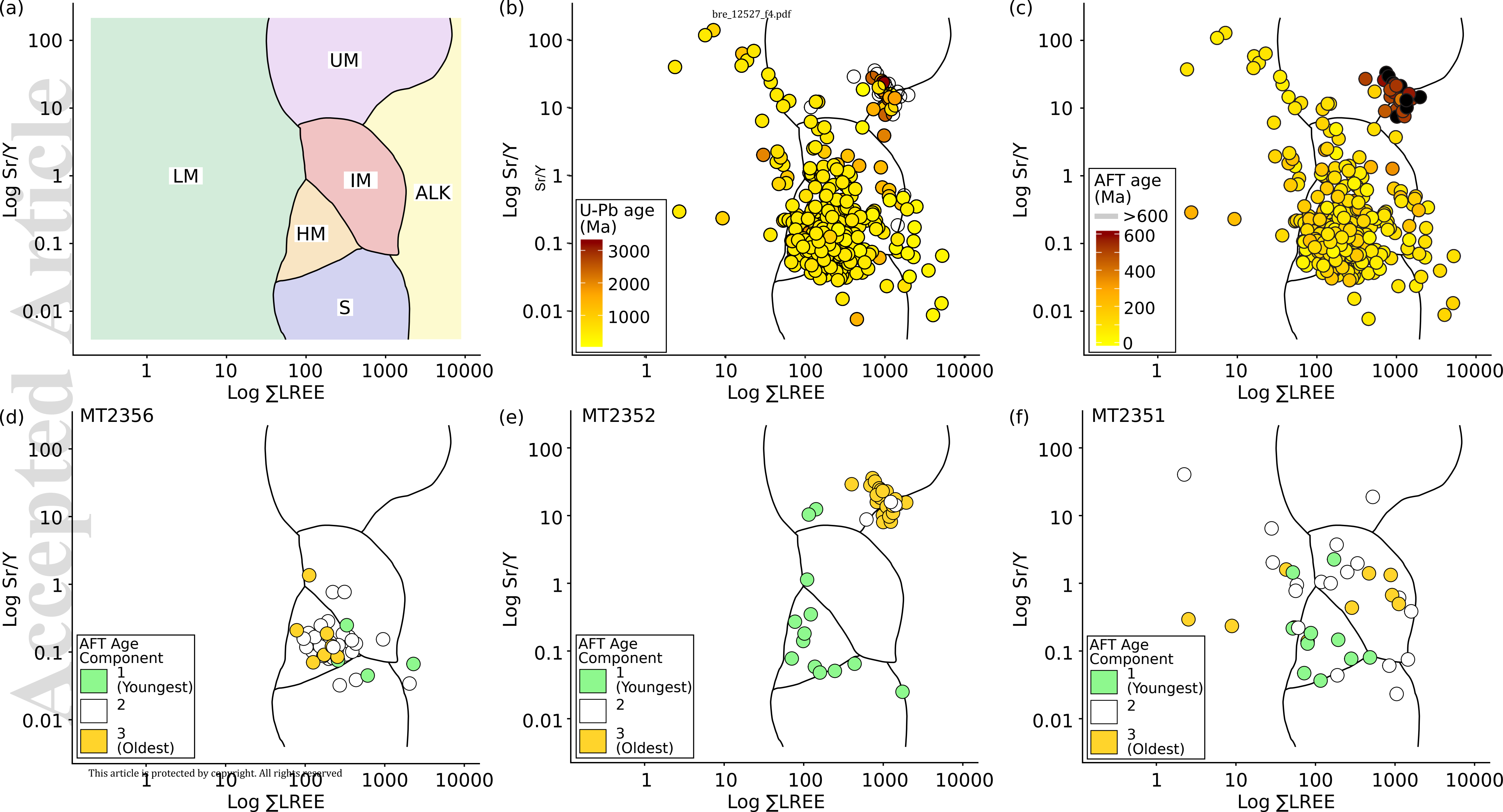


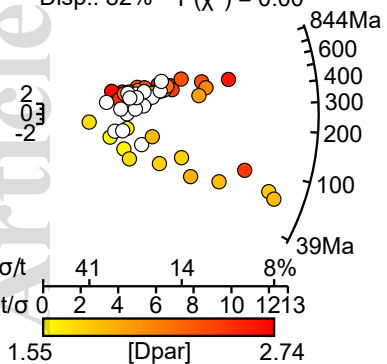
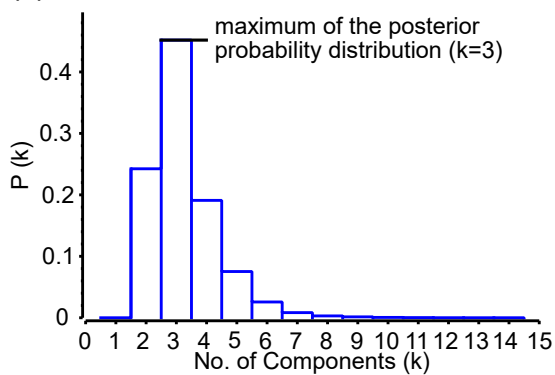
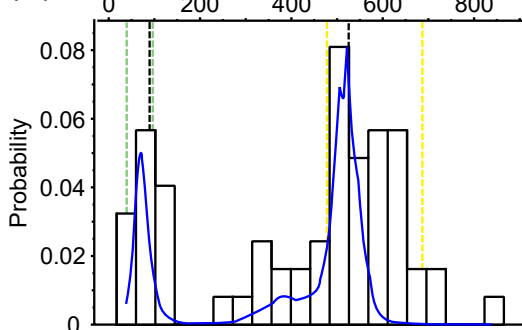
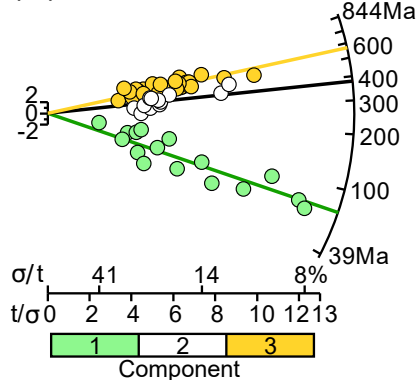
This article is protected by copyright. All rights reserved



This article is protected by copyright. All rights reserved



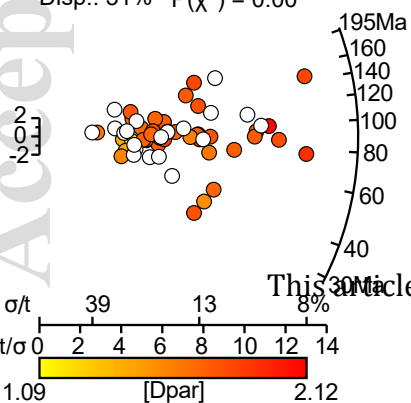
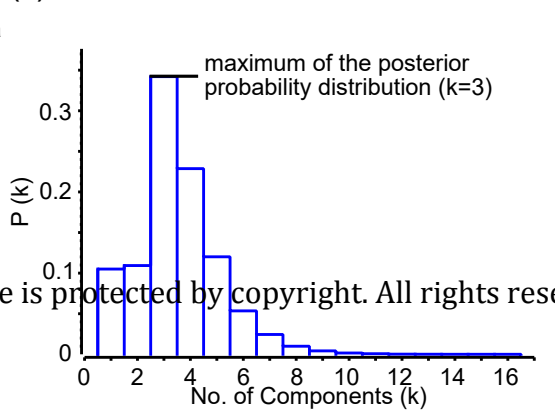
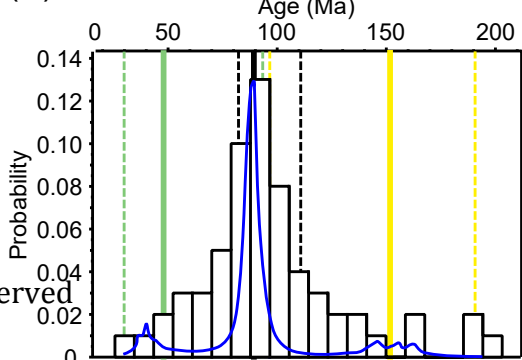
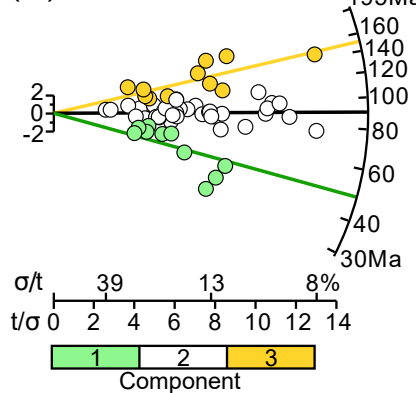


(a) MT2352 (#XtIs = 63, #CTs = 328)**(i)** C. Age: 317 ± 33 Ma (1σ)
Disp.: 82% $P(\chi^2) = 0.00$ **(ii)****(iii)** bre_12527_f5.pdf Age (Ma)**(iv)**

k = 1 #XtIs = 16 #CTs = 64
C. AFT age = 77.2 ± 6.4 Ma
 $P(\chi^2) = 0.00$ Disp. = 27 %
MTL = 12.5 ± 1.5 μm
Dpar = 1.82 ± 0.24 μm

k = 2 #XtIs = 12 #CTs = 41
C. AFT age = 392.2 ± 20.3 Ma
 $P(\chi^2) = 0.54$ Disp. = 1 %
MTL = 12.6 ± 1.5 μm
Dpar = 2.05 ± 0.07 μm

k = 3 #xtIs = 35 #CTs = 223
C. AFT age = 570.5 ± 18.0 Ma
 $P(\chi^2) = 0.99$ Disp. = 0 %
MTL = 12.6 ± 1.5 μm
Dpar = 2.05 ± 0.07 μm

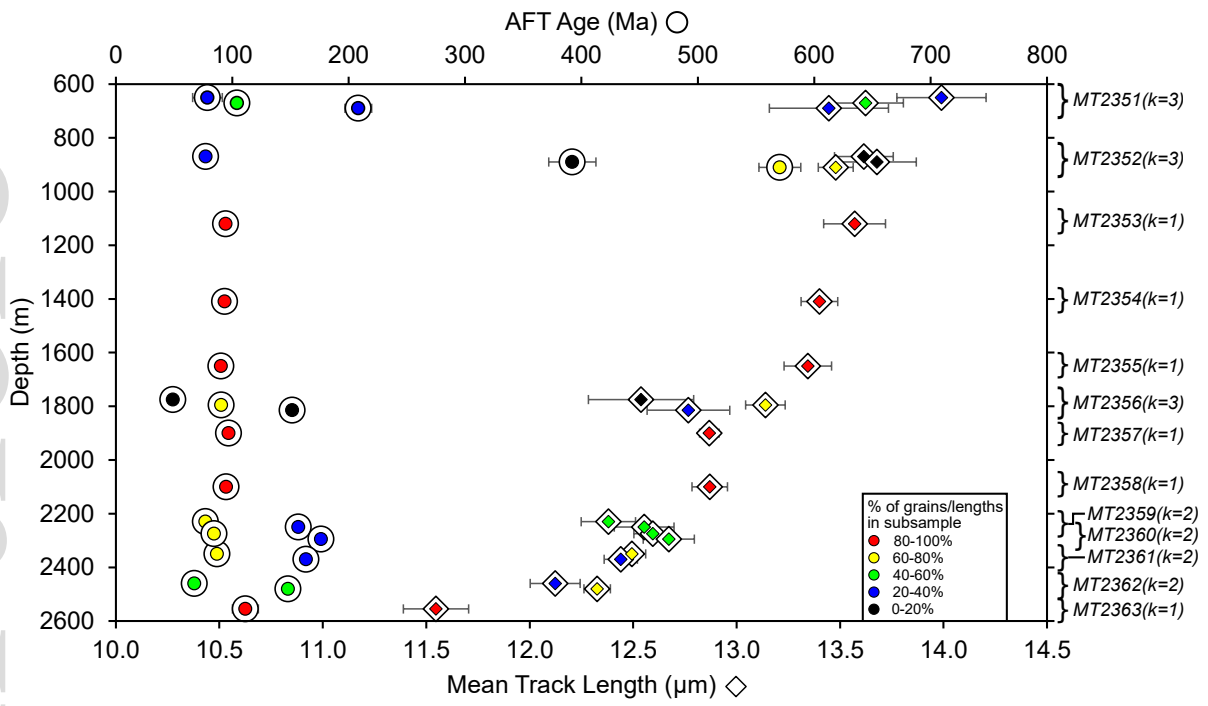
(b) MT2356 (#XtIs = 63, #CTs = 152)**(i)** C. Age: 92.5 ± 4 Ma (1σ)
Disp.: 31% $P(\chi^2) = 0.00$ **(ii)****(iii)****(iv)**

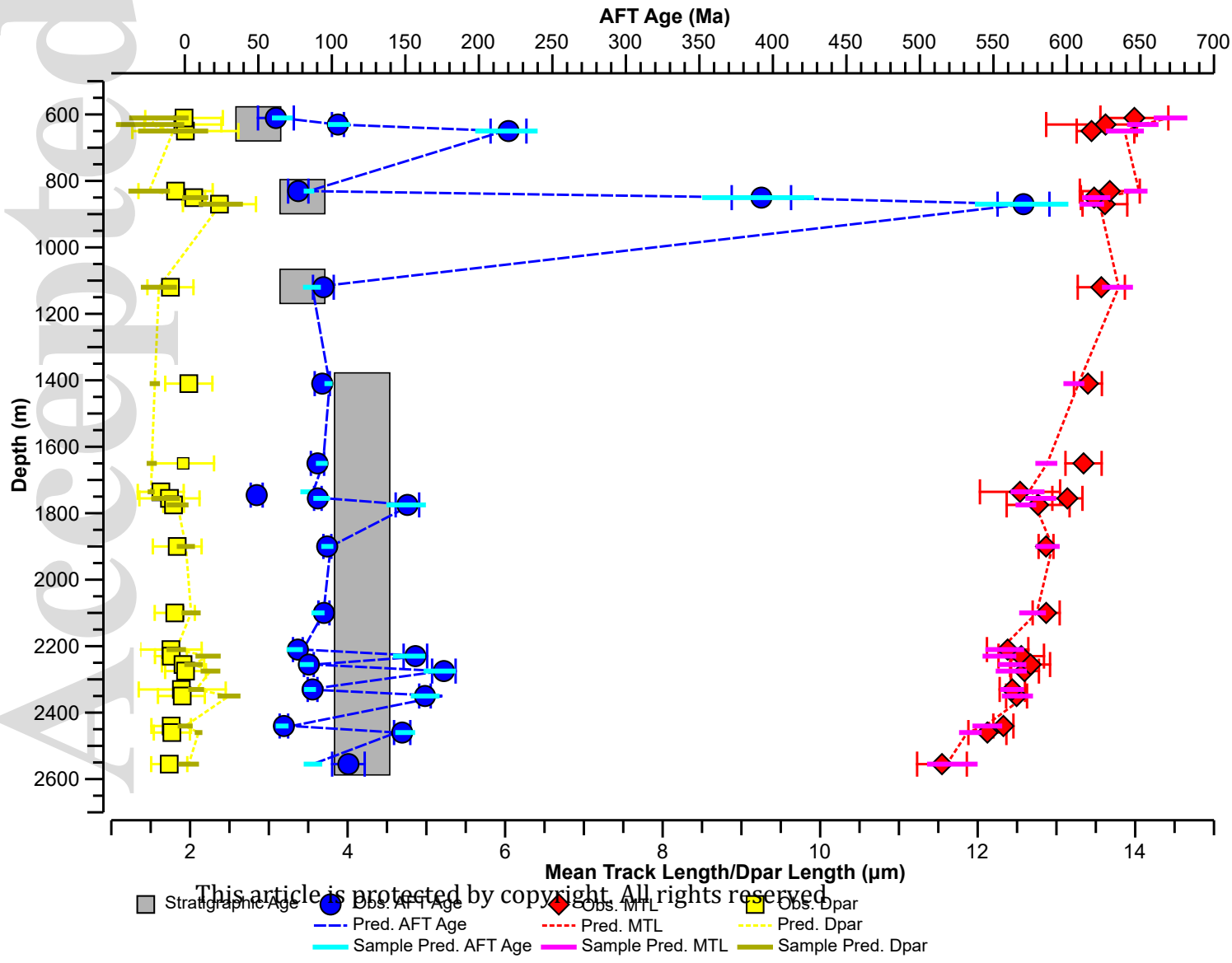
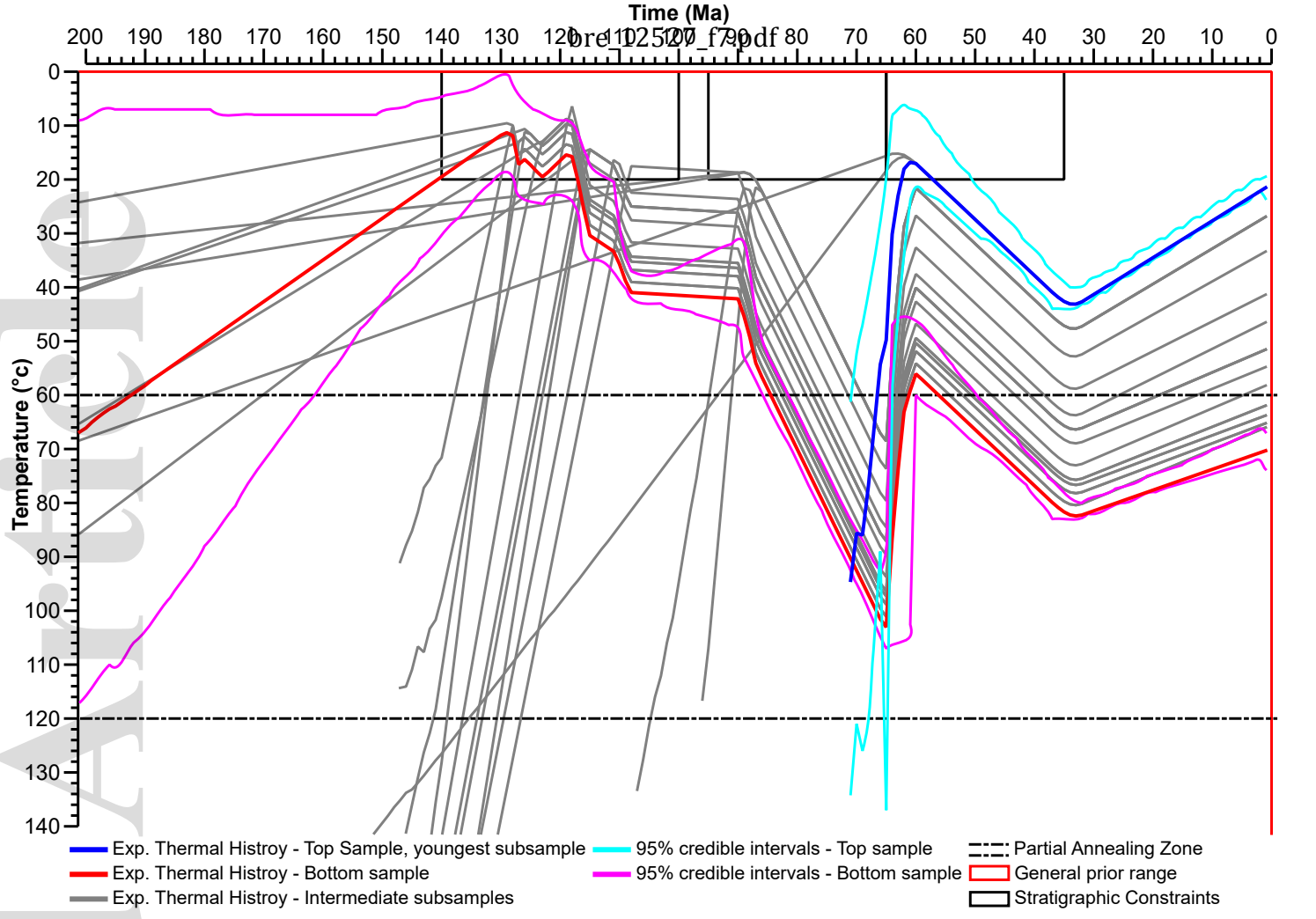
k=1 #XtIs = 10 #CTs = 17
AFT age = 48.9 ± 4.1 Ma
 $P(\chi^2) = 0.33$ Disp. = 19 %
MTL = 11.1 ± 1.3 μm
Dpar = 1.63 ± 0.15 μm

k=2 #XtIs = 42 #CTs = 103
AFT age = 90.5 ± 2.3 Ma
 $P(\chi^2) = 0.92$ Disp. = 2 %
MTL = 11.8 ± 1.4 μm
Dpar = 1.74 ± 0.20 μm

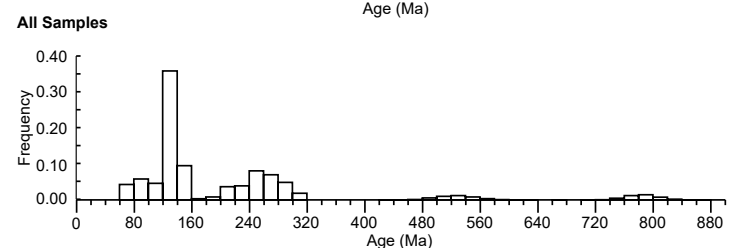
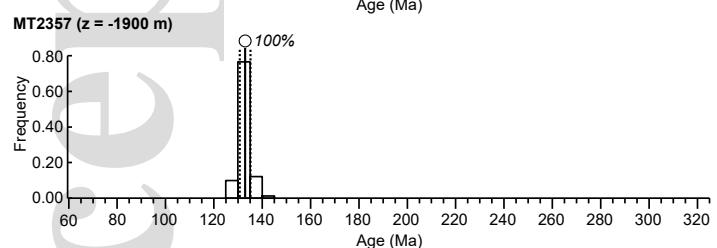
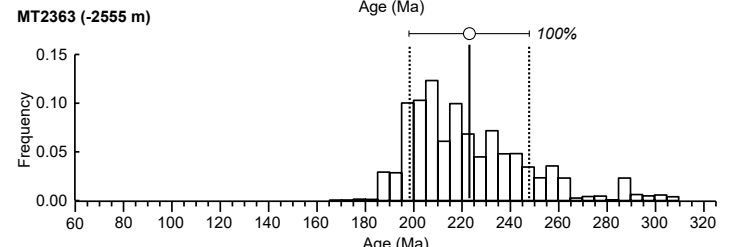
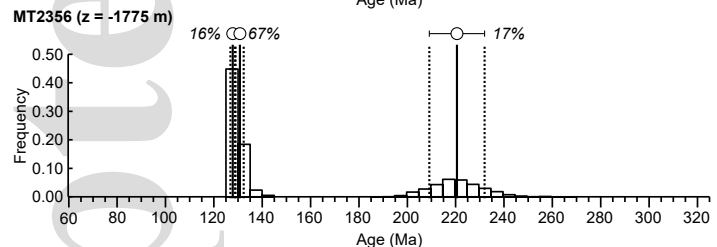
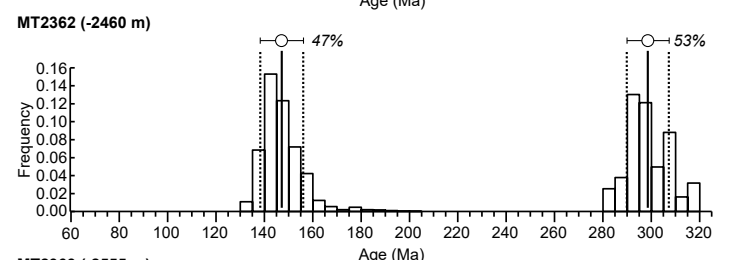
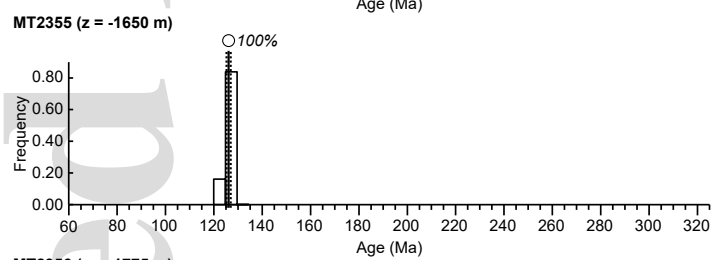
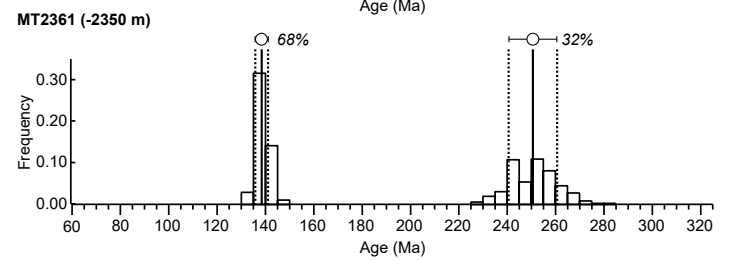
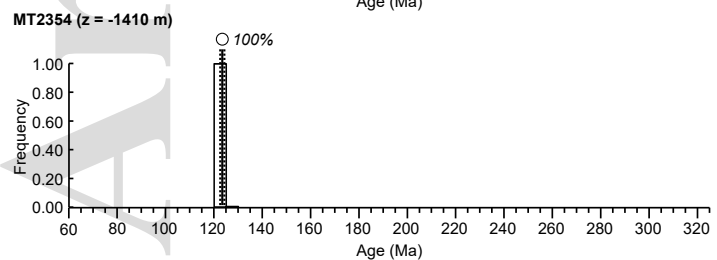
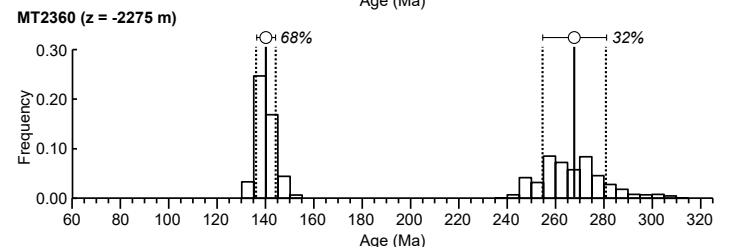
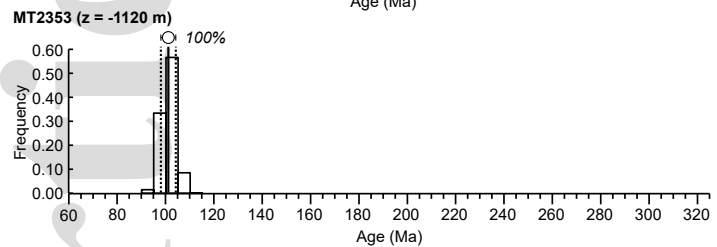
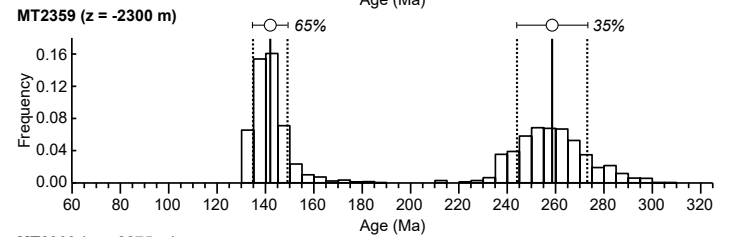
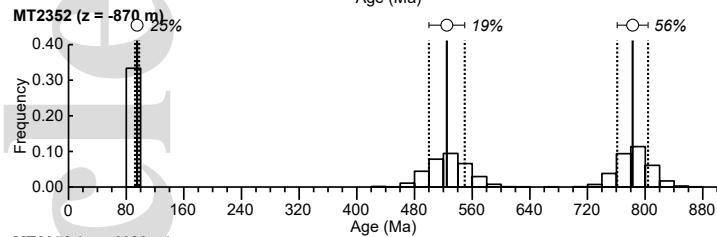
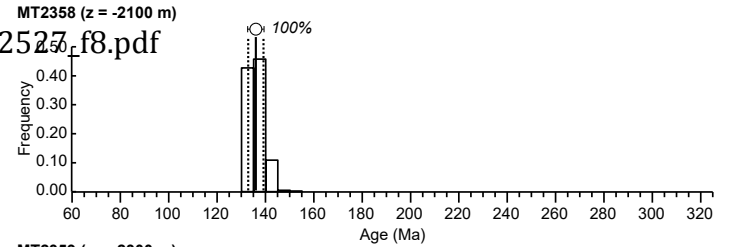
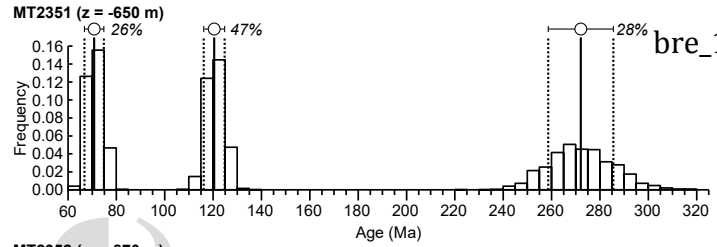
k=3 #XtIs = 11 #CTs = 32
AFT age = 151.4 ± 8.0 Ma
 $P(\chi^2) = 0.15$ Disp. = 9 %
MTL = 12.6 ± 1.5 μm
Dpar = 2.05 ± 0.07 μm

This article is protected by copyright. All rights reserved

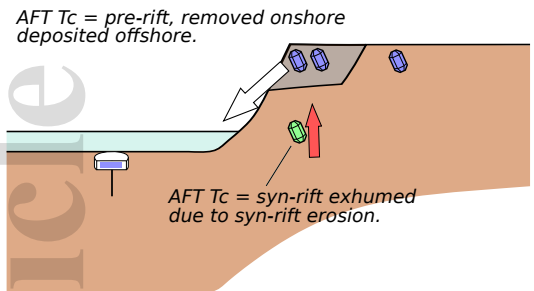




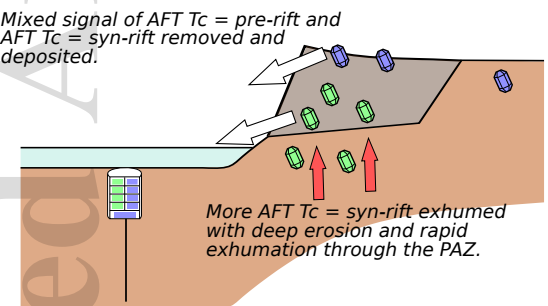
This article is protected by copyright. All rights reserved.



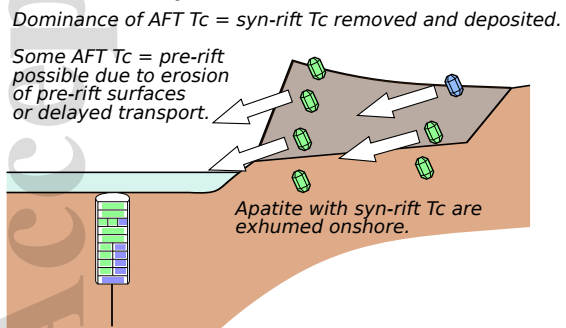
(a) Start of Syn-rift 145 - 125 Ma



(b) Syn-rift 145 - 125 Ma

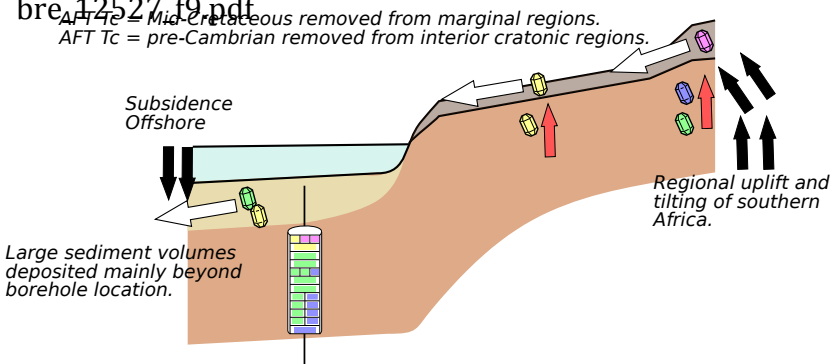


(c) End of Syn-rift 145 - 125 Ma

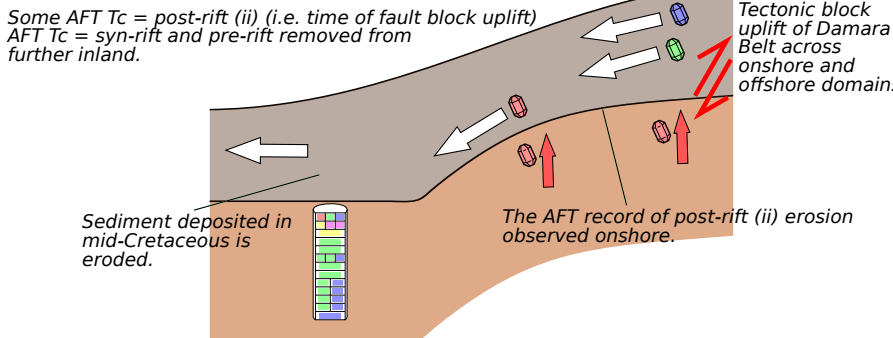


(d) Post-Rift (i) 110 - 80 Ma

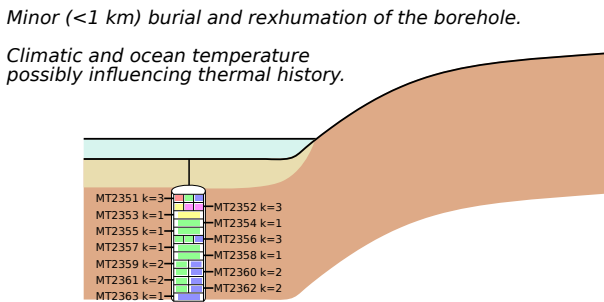
bre.12527.f9.pdf



(e) End Post-rift (ii): 65 - 60 Ma



(f) Cenozoic - Present day



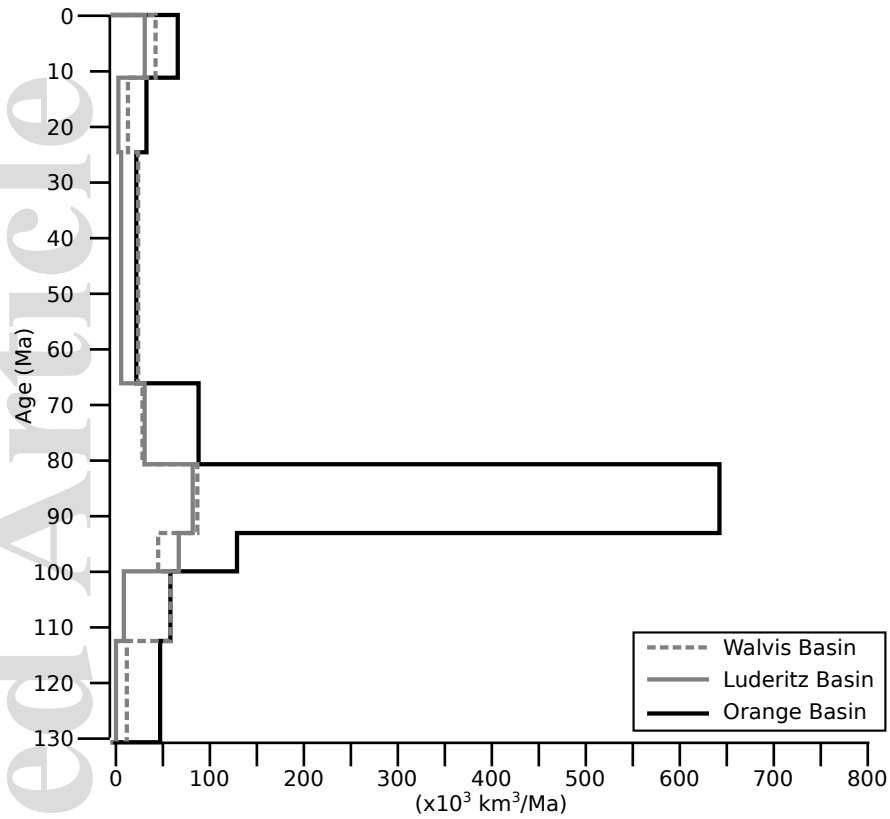
- Post-rift: 60 - 80 Ma
- Post-rift: 90 - 110 Ma
- Syn-rift: 125 - 145 Ma
- Pre-rift: 145 - 300 Ma
- Pre-rift: >300 Ma
- Deposited AFT Tc
- Eroded AFT Tc
- Pre-rift AFT Tc
- Pre-rift Tc

- Transportation of eroded apatite grains
- Exhumation of apatite grains
- Vertical movements of crust
- Faulting

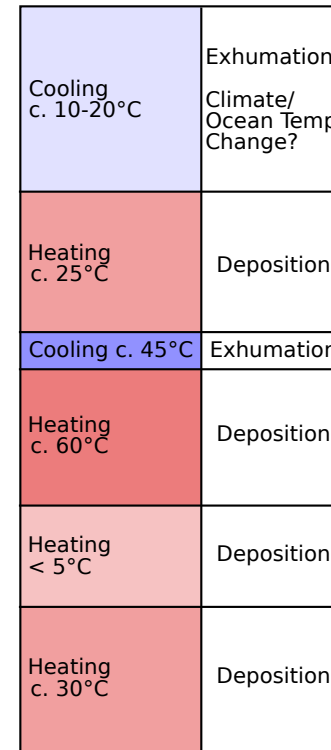
- Eroded section
- Crust
- Deposited sediments
- Sea

This article is protected by copyright. All rights reserved

Sediment Volumes



Thermal history inferred from borehole thermal history.



Regional onshore erosional events inferred from thermochronology.

